



HAL
open science

Composition of conglomerates analyzed by the Curiosity rover: Implications for Gale Crater crust and sediment sources

N. Mangold, L. Thompson, O. Forni, A. Williams, C. Fabre, Laetitia Le Deit, R. Wiens, R. Williams, R. Anderson, D. Blaney, et al.

► To cite this version:

N. Mangold, L. Thompson, O. Forni, A. Williams, C. Fabre, et al.. Composition of conglomerates analyzed by the Curiosity rover: Implications for Gale Crater crust and sediment sources. *Journal of Geophysical Research. Planets*, 2016, 121 (3), pp.353-387. 10.1002/2015JE004977 . hal-02373381

HAL Id: hal-02373381

<https://hal.science/hal-02373381>

Submitted on 6 Jan 2022

HAL is a multi-disciplinary open access archive for the deposit and dissemination of scientific research documents, whether they are published or not. The documents may come from teaching and research institutions in France or abroad, or from public or private research centers.

L'archive ouverte pluridisciplinaire **HAL**, est destinée au dépôt et à la diffusion de documents scientifiques de niveau recherche, publiés ou non, émanant des établissements d'enseignement et de recherche français ou étrangers, des laboratoires publics ou privés.

Copyright

RESEARCH ARTICLE

10.1002/2015JE004977

Special Section:

The Mars Science Laboratory
Rover Mission (Curiosity) at The
Kimberley, Gale Crater, Mars

Key Points:

- Conglomerates analyzed by Curiosity display two types, both are feldspar rich, one with plagioclase and the second with K feldspar
- Conglomerates chemistry can be used as a proxy for estimating Gale Crater crustal composition
- Differences in chemistry between conglomerates and finer-grained deposits highlight variations due to Mg fluids and physical sorting

Correspondence to:

N. Mangold,
nicolas.mangold@univ-nantes.fr

Citation:

Mangold, N., et al. (2016), Composition of conglomerates analyzed by the Curiosity rover: Implications for Gale Crater crust and sediment sources, *J. Geophys. Res. Planets*, 121, 353–387, doi:10.1002/2015JE004977.

Received 5 NOV 2015

Accepted 25 FEB 2016

Accepted article online 4 MAR 2016

Published online 16 MAR 2016

Composition of conglomerates analyzed by the Curiosity rover: Implications for Gale Crater crust and sediment sources

N. Mangold¹, L. M. Thompson², O. Forni³, A. J. Williams⁴, C. Fabre⁵, L. Le Deit¹, R. C. Wiens⁶, R. Williams⁷, R. B. Anderson⁸, D. L. Blaney⁹, F. Calef⁹, A. Cousin³, S. M. Clegg⁶, G. Dromart¹⁰, W. E. Dietrich¹¹, K. S. Edgett¹², M. R. Fisk¹³, O. Gasnault³, R. Gellert¹⁴, J. P. Grotzinger¹⁵, L. Kah¹⁶, S. Le Mouélic¹, S. M. McLennan¹⁷, S. Maurice³, P.-Y. Meslin³, H. E. Newsom¹⁸, M. C. Palucis¹¹, W. Rapin³, V. Sautter¹⁹, K. L. Siebach¹⁵, K. Stack⁹, D. Sumner²⁰, and A. Yingst⁷

¹Laboratoire de Planétologie et Géodynamique de Nantes, CNRS, UMR 6112, Université de Nantes, Nantes, France, ²Planetary and Space Science Centre, Department of Earth Sciences, University of New Brunswick, Fredericton, New Brunswick, Canada, ³Institut de Recherche en Astrophysique et Planétologie, CNRS/Université de Toulouse, UPS-OMP, Toulouse, France, ⁴Department of Physics, Astronomy, & Geosciences, Towson University, Towson, Maryland, USA, ⁵GéoRessources, Université de Lorraine, Nancy, France, ⁶Los Alamos National Laboratory, Los Alamos, New Mexico, USA, ⁷Planetary Science Institute, Tucson, Arizona, USA, ⁸USGS, Flagstaff, Arizona, USA, ⁹Jet Propulsion Laboratory, California Institute of Technology, Pasadena, California, USA, ¹⁰Laboratoire de Géologie de Lyon, Université de Lyon, Lyon, France, ¹¹Department of Earth and Planetary Science, University California, Berkeley, California, USA, ¹²Malin Space Science Systems, San Diego, California, USA, ¹³College of Earth, Ocean, and Atmospheric Sciences, Oregon State University, Corvallis, Oregon, USA, ¹⁴Department of Physics, University of Guelph, Guelph, Ontario, Canada, ¹⁵Division of Geological and Planetary Sciences, California Institute of Technology, Pasadena, California, USA, ¹⁶Department of Earth and Planetary Sciences, University of Tennessee, Knoxville, Tennessee, USA, ¹⁷Department of Geosciences, State University of New York at Stony Brook, Stony Brook, New York, USA, ¹⁸Institute of Meteoritics, Department of Earth and Planetary Sciences, Albuquerque, New Mexico, USA, ¹⁹IMPMC, Museum National d'Histoire Naturelle de Paris, France, ²⁰Department of Earth and Planetary Sciences, University of California, Davis, California, USA

Abstract The Curiosity rover has analyzed various detrital sedimentary rocks at Gale Crater, among which fluvial and lacustrine rocks are predominant. Conglomerates correspond both to the coarsest sediments analyzed and the least modified by chemical alteration, enabling us to link their chemistry to that of source rocks on the Gale Crater rims. In this study, we report the results of six conglomerate targets analyzed by Alpha-Particle X-ray Spectrometer and 40 analyzed by ChemCam. The bulk chemistry derived by both instruments suggests two distinct end-members for the conglomerate compositions. The first group (Darwin type) is typical of conglomerates analyzed before sol 540; it has a felsic alkali-rich composition, with a $\text{Na}_2\text{O}/\text{K}_2\text{O} > 5$. The second group (Kimberley type) is typical of conglomerates analyzed between sols 540 and 670 in the vicinity of the Kimberley waypoint; it has an alkali-rich potassic composition with $\text{Na}_2\text{O}/\text{K}_2\text{O} < 2$. The variety of chemistry and igneous textures (when identifiable) of individual clasts suggest that each conglomerate type is a mixture of multiple source rocks. Conglomerate compositions are in agreement with most of the felsic alkali-rich float rock compositions analyzed in the hummocky plains. The average composition of conglomerates can be taken as a proxy of the average igneous crust composition at Gale Crater. Differences between the composition of conglomerates and that of finer-grained detrital sediments analyzed by the rover suggest modifications by diagenetic processes (especially for Mg enrichments in fine-grained rocks), physical sorting, and mixing with finer-grained material of different composition.

1. Introduction and Context

Early observations by the Curiosity rover in Gale Crater revealed isolated outcrops of cemented gravel and sand size grains with textures typical of fluvial conglomerates [Williams *et al.*, 2013]. These conglomerates occur as local outcrops on a hummocky plain that has a surface mainly covered by a residual lag composed of clasts and sand. Then, the rover entered into a region named Yellowknife Bay where exposed sedimentary rocks (mudstones and sandstones) were interpreted as fluvial and lacustrine deposits [Grotzinger *et al.*, 2014; McLennan *et al.*, 2014]. After leaving Yellowknife Bay, the rover started a long period of traverse to the main mission objective, the basal layers of Aeolis Mons (known informally as Mount Sharp), the edge of which was reached at a site called Pahrump Hills on sol 750 [Grotzinger *et al.*, 2015]. During this traverse, the rover crossed more hummocky plains, encountered additional conglomerate outcrops, and stopped at the Kimberley field site (sols 600–640).

Among sedimentary rocks, conglomerates are those which are the least altered and provide the most direct knowledge of the source of sediments [e.g., *Seiders and Blome*, 1988; *Cox and Lowe*, 1995]. Preserved clasts enable a direct look at the texture and composition of the source rock. This study aims to analyze the chemistry of conglomerates in order to understand the variability in composition of the source rocks and their relevance for understanding the Martian crust. Conglomerates are also a fundamental link between the source rocks and the finer-grained sediments (i.e., sandstones and mudstones analyzed at our field sites Yellowknife Bay, Kimberley, and Pahrump Hills). This study is focused on observations taken between landing and the arrival at Mount Sharp (from the landing to sol 800, Figure 1). A detailed description of stratigraphy and sedimentary facies for all sediments visited by the rover can be found in *Grotzinger et al.* [2014] and *Grotzinger et al.* [2015]. Our descriptions (section 2) will focus on the depositional setting and texture of the conglomerates to provide a visual context to chemical analyses. Following these observations, we present the chemistry of the conglomerates determined by the Alpha-Particle X-ray Spectrometer (APXS) and ChemCam laser-induced breakdown spectrometer (LIBS) instruments (section 3). In spite of the lack of drill samples from the conglomerates, and thus mineralogical data from CheMin, the identification of mineral phases in some local cases is possible from ChemCam chemical analyses. Specific attention is thus given to the composition of pebbles and individual grains in the conglomerates. We compare these data with finer-grained fluvial and lacustrine sediments analyzed by the rover as well as random float rocks observed in the hummocky plains (section 4). The discussion further develops scenarios for the formation of conglomerates from crustal sources and evaluates their differences with finer-grained sediments (section 5).

2. Geological Observations

2.1. Methods

Imaging for geological observations is provided by three instruments: (i) MastCam, with two cameras located on the mast of the rover; (ii) ChemCam/Remote Micro-Imager (RMI), which takes context images for ChemCam chemical data, also located on the mast; and (iii) Mars Hand Lens Imager (MAHLI), which focuses on the texture and is located on the arm (see Appendix A for more details on instrumental techniques). To resolve a grain requires a minimum of 3 pixels (although 5 pixels may be necessary to actually quantify grain size; see Appendix B). Based on instrument capabilities, MAHLI images enable us to observe grains down to 0.042 mm at best, ChemCam/RMI down to 0.120 mm (at 2 m distance), and MastCam-R grains of 0.250 mm (at 2 m distance). Thus, we were not always able to determine the presence and extent of the finest populations of grains.

The variability in distances of image acquisition and the limited use of the arm (and consequently of MAHLI imagery) prevent systematic analyses of grain sizes. Three local analyses are provided as examples (Appendix B). The variability in distance also prevents characterization of sediments at the same scale. For instance, a statistical distribution could classify some of them as (pebbly) very coarse sandstone with resolution imagery, but they could be classified as coarser material in lower resolution imagery (see Appendix B for more explanations). Thus, conglomerates were defined qualitatively from the observation of pebbles and not by strict control of grain size according to Wentworth scale [Wentworth, 1922]. Similarly, rounding is only qualitatively examined and would require in-depth analyses. *Szabo et al.* [2015] recently proposed a detailed investigation of rounding on only a few selected examples of conglomerates at Gale Crater. Such an effort is out of the scope of the present section which aims to give an overview of the conglomerate texture before more in-depth analysis of the chemistry.

2.2. Stratigraphy of Conglomerates and Target Selection Strategy

Conglomerates were found predominantly as local outcrops in the regolith-covered hummocky plains (Figure 1). Characterizing the stratigraphy was not straightforward due to the presence of these hummocky plains limiting the occurrence of stratigraphic contacts (Figure 1). As the dip of most of the strata is subhorizontal, the elevation was used as an approximation to the stratigraphic position in areas of poor rock exposure [Grotzinger et al., 2015]. In this interpretation, conglomerates were progressively observed less frequently while finer-grained sandstones and mudstones were observed more frequently upsection (Figures 1b and 1c). This fining-up sequence is consistent with the increasing distance from the Gale Crater rim in an alluvial-lacustrine environment [Grotzinger et al., 2015].

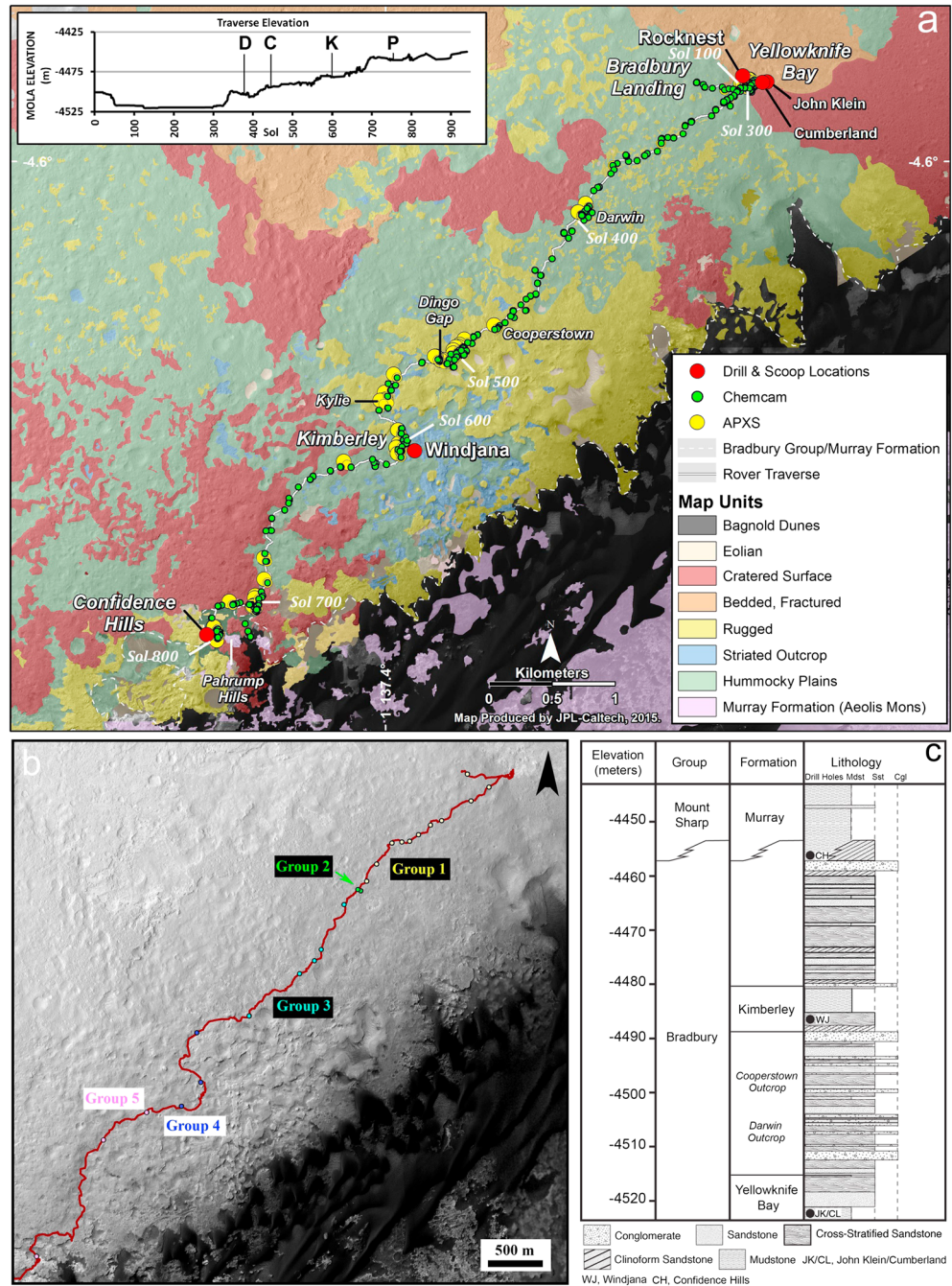


Figure 1. (a) Surface terrain map of the Curiosity rover traverse from the Bradbury Landing site to the Pahrump Hills at the foot of Mount Sharp (adapted from Grotzinger *et al.* [2014]). The geological map was constructed based largely on High Resolution Imaging Science Experiment (HiRISE) images and used to demarcate major terrain types, thus corresponding to orbital facies rather than actual geological units. The topographic profile at the top indicates the major outcrops: D = Darwin, C = Cooperstown; K = Kimberley; and P = Pahrump. (b) HiRISE mosaic with rover traverse and locations with conglomerates analyzed in the study. (c) Stratigraphic column, adapted from Grotzinger *et al.* [2015].

Most of the outcrops were analyzed as a consequence of opportunistic science, i.e., data acquired during the traverse without prolonged stops for contact science (close-up analyses using the arm) or sample extraction and analysis. The implication is that most of the observations of conglomerates were obtained by remote sensing instruments, i.e., MastCam and ChemCam, and that the target selection was not achieved according to a systematic sampling campaign. The conglomerates were not drilled, because the texture was not

favorable for drilling and because organics—a major goal of Curiosity—are not expected to be stored and preserved long term in such rocks. Nevertheless, one location chosen from orbital images, and named the Darwin waypoint, was the object of longer activities during sols 390 to 400. The Darwin campaign enabled the use of the robotic arm to acquire MAHLI and APXS data for more detailed analyses of texture and chemistry.

According to stratigraphy and the sampling strategy, we separate the conglomerate observations into five groups. The first three groups correspond to isolated outcrops on the hummocky plains. We have separated the Darwin observation (sol 390–400) from previous observations (< sol 390) and subsequent observations (sol 390–540) because Darwin was studied in much more detail. This means that we have a good statistical sampling of the chemistry of Darwin. In contrast, we have poor statistics for other individual outcrops observed along the traverse but, together, they build a meaningful data set for the chemistry of conglomerates encountered in the hummocky plains. After Dingo Gap (sol 540, Figure 1), we grouped the conglomerates of the Kylie-Kimberley area together because they were found as basal strata of sandstones that were analyzed in detail at Kimberley [e.g., *Treiman et al.*, 2016]. Since leaving Kimberley, the rover has not crossed many conglomerate outcrops (see stratigraphic column, Figure 1), so we have grouped post-Kimberley conglomerates together to enable a better statistical sampling. Note also that we have been conservative in the selection of conglomerates: a few more outcrops were considered as potential conglomerates, but they were not selected because of poor preservation or strongly weathered textures.

2.3. Description of Conglomerate Outcrops Along the Rover Traverse

2.3.1. Conglomerates in the Hummocky Plains Before the Darwin Outcrop (Sols 1–390)

The first conglomerate outcrops encountered by Curiosity were isolated, well-indurated in-place blocks containing pebbles up to 4 cm in diameter [*Williams et al.*, 2013]. These conglomerates were observed on the Bradbury Rise in the immediate vicinity (<200 m) of the landing site before reaching Yellowknife Bay. At Yellowknife Bay (during sols 60–330), only sandstones and mudstones were observed [*Grotzinger et al.*, 2014; *Mangold et al.*, 2015]. The majority of pebbles within these conglomerates have a subrounded to rounded shape and range in color or tone from black to grey to white and translucent. Locally, there were examples of imbricated clasts and parallel stratification with pebble-rich layers [*Williams et al.*, 2013]. To transport these pebbles, sediments were interpreted as having been mobilized in water flows with depths of 0.03 to 0.9 m [*Williams et al.*, 2013]. Only the target Link (sol 27, five points) was analyzed by ChemCam during this initial traverse [*Williams et al.*, 2013; *Yingst et al.*, 2013]. The composition of Link is consistent with a predominance of feldspathic minerals, with limited water interaction [*Williams et al.*, 2013].

Progressing out of Yellowknife Bay (sols 330–390), the hummocky plains displayed limited outcrop exposures with no well-exposed sections. However, all observed outcrops comprised conglomerates, spanning an elevation range of approximately 25 m (Figure 1). Figure 2 displays an area typical of the hummocky plains. These plains are dominated by a residual lag of sand and clasts, but local outcrops are identifiable as patches of light-toned material in the rover navigation cameras (NavCam) (Figure 2a). The RMI images of these rocks permit identification of grains typically down to ~0.5 mm (Figures 2d and 2e). At this scale, it is not always possible to determine whether the matrix is composed of sand grains finer than 0.5 mm in diameter or smaller particles, but the conglomerate is clast supported with a limited proportion of grains finer than 0.5 mm (Figure 2e). The larger observed clasts reach 6 cm. Many clasts appear rounded to subrounded, especially those at the centimeter scale (white arrows in Figure 2e).

Before arriving at the Darwin waypoint, Curiosity stopped to do contact science (MAHLI and APXS) at a 6 cm diameter pebble target named Ruker (sol 385) (Figure 3). The outcrop around Ruker is composed of a poorly exposed conglomerate with angular to subangular granules, cobbles, and pebbles of various tones (Figures 3a and 3b). Interest in this outcrop was largely triggered by the Ruker clast on which ChemCam/RMI and MAHLI images were taken (Figures 3c and 3d). This clast has a predominantly dark texture with occurrence of white phenocrysts, commonly with anhedral texture but with some of them displaying euhedral texture showing straight edges (black arrow in Figure 3d), indicating an igneous origin.

2.3.2. Conglomerates at the Darwin Outcrop (Sols 390–401)

The ~4 m thick Darwin outcrop (Figure 4) is characterized by 10–50 cm thick conglomerates limited by several centimeter-thick interbeds of fine-grained sandstones [*Williams et al.*, 2014; *Stack et al.*, 2014]. In the middle of a 20 cm high ledge is the target named Altar Mountain, exhibiting clasts ranging from <1 mm to 2.5 cm in

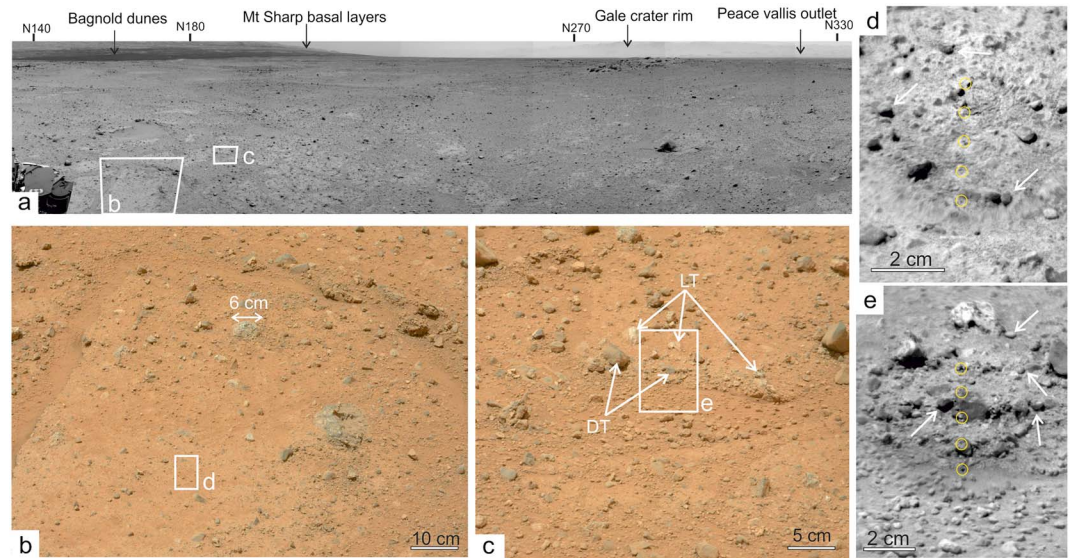


Figure 2. Outcrop of conglomerates typical of outcrops inside hummocky plains (sol 363). (a) Navcam mosaic showing how light-toned outcrops were identified during planning. (b and d) Target Labyrinth Lake viewed by MastCam image (0363ML1475001000E1_DXXX) and ChemCam (CR0_429711813PRC_F0120244CCAM01363L2). (c and e) Close-up of Buit Lake with MastCam (0363MR1476001000E_DXXX) and ChemCam (CR0_429712639PRC_F0120244CCAM02363L2 and CR0_429713215PRC_F0120244CCAM02363L2). DT: dark-toned clast. LT: light-toned clast. Yellow circles, here and in the following figures, indicate the exact locations of ChemCam points. White arrows in Figures 2d and 2e indicate rounded clasts.

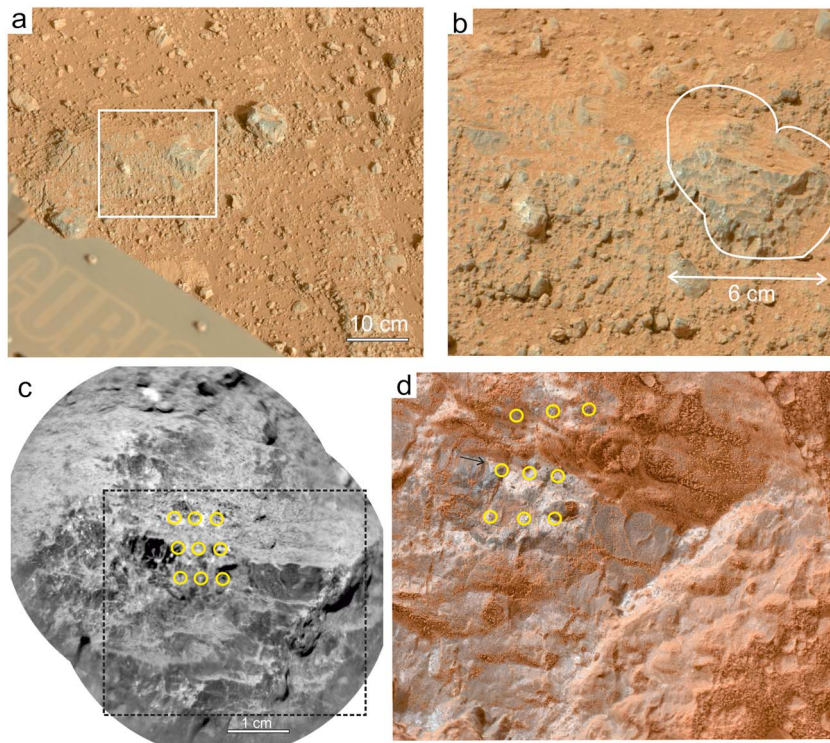


Figure 3. (a) Small outcrop of conglomerates encountered before reaching the Darwin outcrop, sol 385 (MastCam 0385ML001581000200335E01_DXXX). (b) Close-up of the 6 cm wide pebble Ruker embedded inside the conglomerate (MastCam 0387MR1594001000E1_DXXX). (c) ChemCam RMI image of Ruker with the nine locations analyzed (ChemCam images CR0_4318477353PRC_F0150998CCAM05387L2 and CR0_431848433PRC_F0150998CCAM05387L2). (d) MAHLI image composite (cropped from a mosaic of focus merge products 387MH0001710000104365R00 and 0387MH000171000104369R00) of Ruker (different view angle).

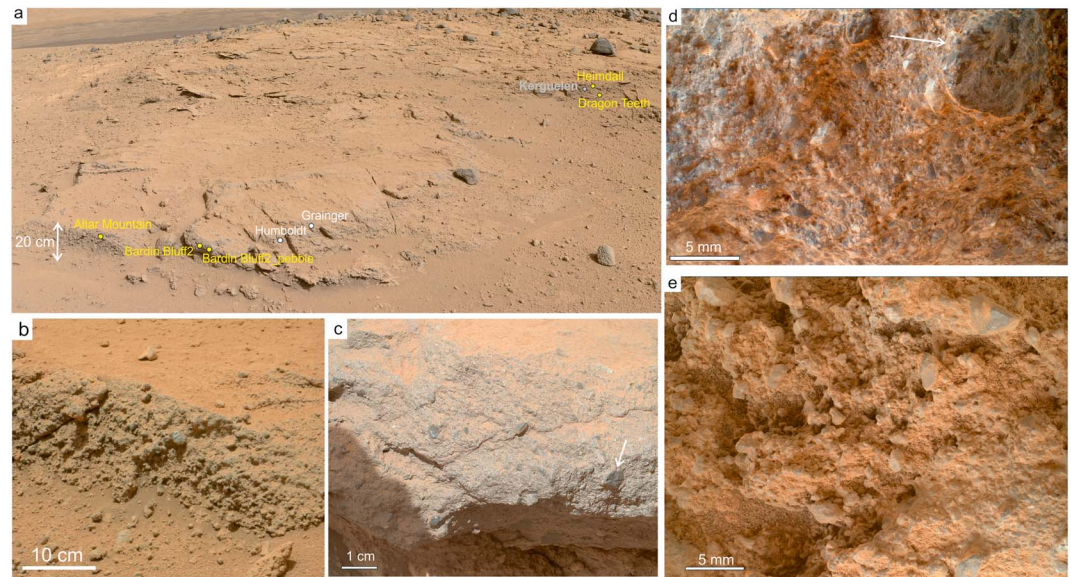


Figure 4. Images of the conglomerates of Darwin outcrop (sol 390). (a) Mosaic of MastCam images 0390ML160700n000E1_DXXX with n from 0 to 9. White dots indicate ChemCam only targets. Grey dot indicates APXS-only targets. Yellow dots indicate common APXS and ChemCam targets. (b) Close-up of the Altar Mountain target (MastCam image 0392MR161500000E1_DXXX). (c) Close-up on the Bardin Bluff target (mosaic of MAHLI images 0394MH0001900010104375C00 and 0394MH0001900010104407C00). The arrow to the right of the image indicates the rounded pebble over which APXS was centered and on which ChemCam shot one point of a 3×3 matrix. Note that the pebble diameter is 0.6 cm, thus much less than the APXS footprint (1.7 cm). (d) Close-up (5 cm standoff) of the area with the 6 mm pebble at Bardin Bluff. The surface is relatively dust free and displays a grain-supported texture, with grains visible down to ~ 0.1 mm. No patch of cement is visible between grains suggesting a limited contribution (MAHLI image 0396MH0001700000104470R00). (e) Close-up (6 cm standoff) at Dragons Teeth (MAHLI image 0399MH0003180000104728R00). The surface appears dustier with frequent dust clumps. At the lower right, the texture appears grain supported but dust clumps collected in the holes between grains hide a possible contribution from cements.

diameter (Figure 4b). The facies is grain supported and shows no preferred grain orientation. Clasts are embedded in a sandy matrix and are subangular to subrounded in shape.

Immediately to the right of the Altar Mountain bed (Figure 4c) is the Bardin Bluffs conglomerate, a massive layer that appears to fine upward. Moderately rounded fine pebbles (typical diameter < 1 cm) are in a sandy (1 mm diameter) matrix with a clast-supported fabric. The Bardin Bluffs layer is more resistant to erosion than Altar Mountain. Overlying Bardin Bluff, and a few meters south of it, is another outcrop of conglomerate that includes the Dragons Teeth and Heimdall targets (Figure 4a, to the right). This conglomerate is similar to Altar Mountain in texture with frequent pebbles several centimeters in diameter (~ 5 to 10 each 10×10 cm). This outcrop is also characterized by several prominent fracture fills that crosscut the surface subvertically. This study reports on the bulk rock composition of this area and does not describe the composition of the fracture fills observed there.

To provide a more in-depth observation of these outcrops, we used MAHLI images to describe qualitatively and quantitatively the grain distribution at the Darwin outcrop (Figure 4d and Appendix B). Based on these observations, the Bardin Bluff target is a pebbly very coarse sandstone based on the average grain size (1.17 mm), but we classified it as a conglomerate because a coarser resolution would not have enabled identification of the smallest particles, as explained in section 2.1. This rock is composed of light- and dark-toned clasts. Clasts are rounded to subrounded. The Dragons Teeth target (Figure 4e) is a conglomerate with coarser average grain size (2.06 mm), composed of gray and light-toned clasts. Orange particles usually cover many grains and accumulate at grain boundaries as clumps, as typically observed for dust at this scale of observation. The presence of dust limits investigation of matrix. Clasts are subangular to subrounded. Both Dragons Teeth and Bardin Bluff are poorly sorted (see Appendix B).

These two examples have been further studied to estimate the proportion of fines, here corresponding to grains < 0.125 mm, thus including sand, silt, and clay size material, and possible cements. The fraction of grains smaller than 0.125 mm is small in both examples, $< 10\%$ for both targets (see Appendix B for

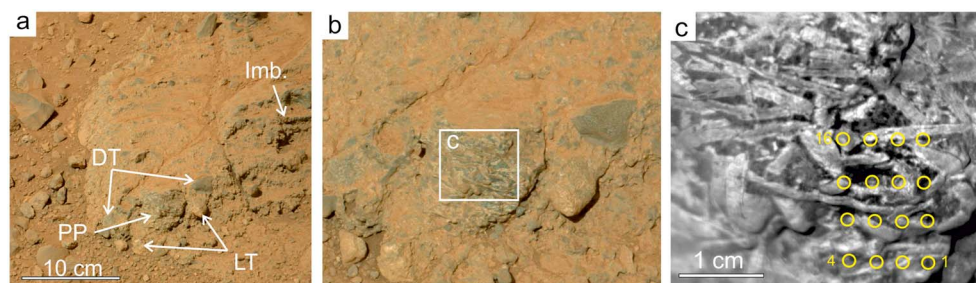


Figure 5. Close-up of the target Harrison, a pebble embedded in conglomerate (sol 512). (a) MastCam image (0512MR201200000E1_DXXX) showing Harrison (PP: Porphyritic pebble), dark-toned pebbles (DT), and light-toned pebbles (LT). Imb indicate imbrication of small pebbles along a layer. (b) MastCam image (0514MR202100000E1_DXXX) and (c) ChemCam RMI image (CR0_443119527PRC_F0250540CCAM02514L1) showing the porphyritic texture of Harrison with long light-toned phenocrysts inside a darker matrix presenting locally dark-toned minerals. The yellow circles indicate the locations of ChemCam chemical analyses.

methodology). In each case, this proportion takes into account fine sand that should not be considered as matrix, strictly speaking, so these proportions are overestimates. Identification of cement patches, identifiable from homogeneous fine-grained pore fills, was not successful for these rocks, suggesting that these conglomerates are clast supported and do not contain an abundant fraction of cement.

2.3.3. Observations in the Hummocky Plains After the Darwin Outcrop (Sols 402–540)

After the Darwin waypoint, conglomerate outcrops were less frequent (Figure 1). From sols 440 to 470, Curiosity explored another field site named Cooperstown that consists of finer-grained material, such as sandstones and pebbly sandstones in which a potassic enrichment was observed [Le Deit *et al.*, 2014]. Of special interest among the few conglomerate outcrops observed later is the target Harrison (sol 514), a large clast within a conglomerate which was analyzed both by MastCam and ChemCam (Figure 5). This clast has a porphyritic texture, with 1–2 cm long white crystals in a darker matrix. This clast was described in more detail in Sautter *et al.* [2015]. The conglomerate containing the clast Harrison displays a large variety of clasts of different tones and textures. Many clasts of this conglomerate are rounded or subrounded. Local layering with possible imbrication of clasts is visible in the MastCam image (Imb in Figure 5a), a characteristic that was observed at Hottah, at the Bradbury Landing site [Williams *et al.*, 2013].

2.3.4. Observations in Kylie-Kimberley Area (Sols 540–640)

After crossing a transverse eolian ridge at Dingo Gap, the rover entered a series of canyons bounded by several meters high scarps made predominantly of sandstones [Vasavada *et al.*, 2014]. Conglomerates were locally observed at the base of these outcrops [Edgar *et al.*, 2014; Le Deit *et al.*, 2015; Grotzinger *et al.*, 2015], although they were only infrequently analyzed by the rover's chemical instruments. Bungle Bungle (sol 550), at the Kylie field site, is one of the conglomerates analyzed in this region. It displays a 10–20 cm thick section with subhorizontal layers of coarse sedimentary rocks bearing pebbles up to 5 cm in diameter (Figure 6). ChemCam and APXS analyzed the target Jum Jum, located at the left edge of this outcrop (Figures 6d and 6e). The Jum Jum target is a conglomerate (average grain size = 3.86 mm, Appendix B) composed of dark-toned clasts and few light-toned clasts in a dark-toned matrix. The surface is physically weathered and appears polished, limiting investigations of smaller grains. Clasts vary from rounded to subangular.

A few hundred meters farther southwest, the Kimberley field site is dominated by siltstones and sandstones that are enriched in potassium compared to all other fine-grained sediments analyzed so far [Thompson *et al.*, 2014; Le Deit *et al.*, 2015; Treiman *et al.*, 2016]. Petaluma and Egan targets represent planar-bedded, granule size conglomerate cropping out in the northern side of the Kimberley site, immediately below the finer-grained deposits. The Lamboo target was analyzed immediately after leaving the Kimberley site and is associated with the same basal conglomerate unit. Hence, all these targets are attributed to the same group.

2.3.5. Observations After Kylie-Kimberley Area (Sols 640–780)

After leaving the Kimberley field site, the rover traversed complex assemblages of rough terrains, valleys with sand fills, and local plateau outcrops, eventually reaching the Pahrump Hills field site. The Pahrump Hills rocks (reached after sol 750) consist predominantly of mudstones with minor lenses of cross-bedded sandstones that were interpreted to be part of the Murray formation, considered to be lacustrine in nature and interpreted as the basal unit of Mount Sharp [Grotzinger *et al.*, 2015]. Conglomerates were not encountered frequently

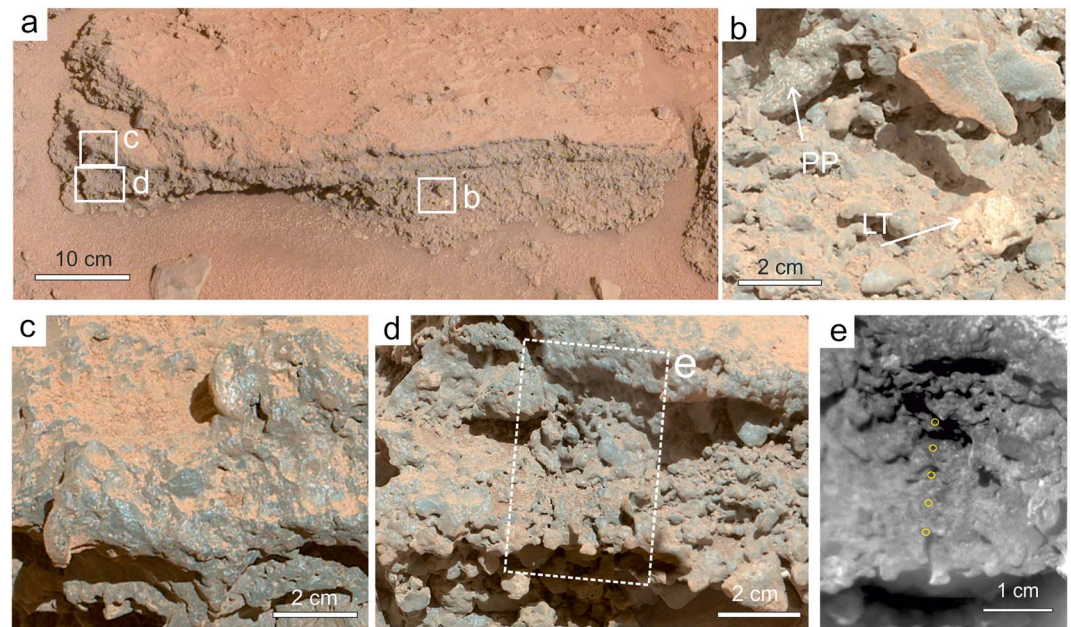


Figure 6. Outcrop Bungle Bungle with the target Jum Jum analyzed by ChemCam and APXS. (a) MastCam of a layered conglomerate outcrop. (b–d) Close-ups on MAHLI images (respectively 0550MH0003520000201602C00, 0550MH0001900010201569C00, and a mosaic of 0550MH0003520000201606C00 and 0550MH0003520000201607C00). LT and PP indicate, respectively, a light-toned pebble and a porphyritic pebble. (e) ChemCam/RMI image of the points of Jum Jum analyzed by ChemCam.

during this part of the traverse. Only one in-place outcrop of conglomerate was analyzed at Podunk (sol 655). The last analysis of conglomerates was performed on sols 775–778 at the target named Bald Mountain. This target is of uncertain stratigraphic position but has been interpreted to underlie the mudstones of the Murray formation based on surrounding conglomerate outcrops not analyzed by ChemCam but observed in imagery from the other rover cameras [Grotzinger *et al.*, 2015].

2.4. Texture of Conglomerate Clasts

The conglomerate grains and clasts observed by imagers along the traverse are in the 2 mm to 6 cm range (Figures 2–5). Fine to very coarse sand grains (0.125–2 mm) are also observed, but the image resolution limits the observation of the finest fraction. For MAHLI images available with a close standoff (<10 cm, as in Figure 4), the proportion of fines is low (<10%) and can be considered as a strict upper bound for any possible cement. Given the lower and varying resolution of RMI images compared to MAHLI images, such a work would require a stand-alone investigation with uncertain results given the results at MAHLI resolution. So no systematic survey was achieved with ChemCam/RMI.

Subangular and angular clasts are common in most conglomerates, but substantial rounding is also frequently observed (e.g., Figures 3c, 3e, 5, and 6) and local imbrication of rounded clasts is observed in the conglomerate around the target Harrison (Figure 5). These conglomerates are also characterized by a diversity of grain colors and tones, suggesting various mineral and rock clasts types. In Figure 2c, grains vary in tone from dark (DT) to light (LT) over a small area (<10 cm in width). Looking at grains individually enables local observations of their internal texture. When visible, this texture shows locally varying light and dark tones, a texture typical of coarse igneous rocks (e.g., 6 cm diameter clast in Figure 2). However, a large number of clasts have a relatively homogeneous grey to dark grey tones suggesting finer-grained texture, possibly corresponding to an aphanitic volcanic texture. These clasts within conglomerates do not show laminations as observed for sedimentary float rocks near Yellowknife Bay [Mangold *et al.*, 2015].

To facilitate mineralogical analyses, we performed a complete survey of all ChemCam/RMI images to observe instances in which the laser hits large individual grains. Eleven such grains were selected (Figure 7), and their chemistry is detailed in section 3.4. These grains vary from dark to light toned with some intermediate tones. Note that the identification of individual grains does not mean that they consist of single-mineral phases;

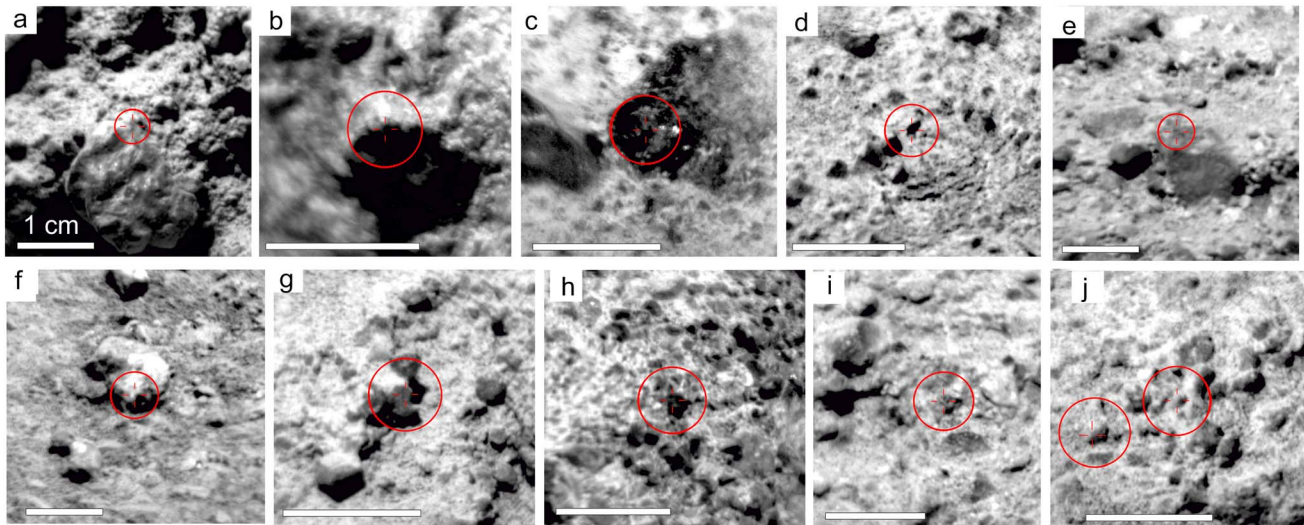


Figure 7. Identification of individual grains using ChemCam/RMI. (a) Altar Mountain point 2: CRO_432290088PRC_F0160000CCAM05392L2. (b) Bardin Bluff2_Pebble point 2: CRO_432645523PRC_F0160050CCAM01394L2. (c) Howey point 3: CRO_428826753PRC_F0110302CCAM02353L1. (d) Labyrinth Lake point 5: CRO_429712411PRC_F0120244CCAM01363L2. (e) Buit Lake point 4: CRO_429712639PRC_F0120244CCAM02363L2. (f) Acme point 6: CRO_429893172PRC_F0120560CCAM03365L1. (g) Heimdall point 1: CRO_433089349PRC_F0160148CCAM02401L1. (h) Deloro point 4: CRO_430422528PRC_F0130292CCAM01371L1. (i) Terra Nova point 5: CRO_430511291PRC_F0130974CCAM01372L1. (j) Radok points 1 (right) and 2 (left): CRO_431132237PRC_F0141132CCAM01379L1. All scale bars are 1 cm.

i.e., some “grains” can correspond to lithic material that will not have the composition of a pure mineral. Nevertheless, by selecting what appear to be individual grains, we improve the chance of analyzing individual minerals.

Individual clasts were also the focus of multiple chemical analyses at Ruker and Harrison. Ruker shows a predominant dark grey color (about 70% of the surface) with a white phase observed in patches. The white phase displays coarser texture with locally angular shapes present (dark arrow in Figure 3d). Conglomerate exposures around the Harrison target contain clasts that vary in tone from very light toned (LT) to dark toned (DT) and from aphanitic to coarse-grained texture (Figure 5b). The 6 cm wide Harrison clast that was analyzed by ChemCam (Figure 5c) shows a porphyritic texture with elongated light-toned grains, consistent with an interpretation as crystal laths (phenocrysts) inside a darker matrix implying an igneous origin [see also *Sautter et al.*, 2015]. At Jum Jum, clast identification is difficult because there are no strong color contrasts between grains. Most observable clasts are dark toned, but light-toned clasts (LT in Figure 6b) exist as well as clasts with mixed light- and dark-toned minerals exhibiting apparent porphyritic textures (PP in Figure 6b).

2.5. Summary and Interpretation

The conglomerates observed by Curiosity exhibit a variety of clast size and angularity, degree of sorting, lithification, and propensity to outcrop. The conglomerates analyzed in the hummocky terrains share textural similarities. The beds tend to be cemented and fractured. Sediment is not well sorted overall but nonetheless displays local imbrication and weak vertical stratification. Subangular grains are common, but so are sub-rounded to rounded sizes (as also mentioned in *Williams et al.* [2013] and *Yingst et al.* [2013]). The deposits are clast supported, and the fine-grained matrix/cement is limited (<10% in the two example images at Darwin considered for their good resolution). The largest conglomerate clasts are up to 6 cm. Overall, these conglomerate characteristics are consistent with an interpretation of fluvial transport and deposition, as first reported at the Bradbury Landing site [*Williams et al.*, 2013]. In contrast, the texture does not match that expected for impact breccia [*Stöffler et al.*, 1979], which usually consists of nonclast-supported material with angular clasts and a large fraction of fine-grained matrix. The prevalent particle rounding, grain-supported deposition, local stratification, and association with sandstones are consistent with gravel bedded river deposits and argue against a pyroclastic flow origin. Likewise, a glacial origin is discounted due to the lack of large boulders as well as striated pebbles usually typical of moraines [e.g., *Leeder*, 1999]. Based on their rounding, *Szabo et al.* [2015] showed that the clasts of some of the conglomerate studied here are interpreted to have been carried tens of kilometers from their source, by bed load transport on an alluvial fan. This is

consistent with an origin for the clasts within the conglomerates as being from the rim and wall of Gale Crater [Palucis *et al.*, 2014; Grotzinger *et al.*, 2015]. Conglomerates therefore provide an opportunity to study the crust exhumed by Gale Crater.

3. Chemistry of Conglomerates From APXS and ChemCam Analyses

3.1. Methods

The ChemCam instrument uses a laser that ablates rocks and provides elemental analysis of rocks or soils, a technique known as LIBS (Appendix A) [Cremers and Radziemski, 1983, 2006; Wiens *et al.*, 2012; Maurice *et al.*, 2012]. Quantification of elements can be accomplished through multivariate or univariate analyses, using, respectively, emission peaks across a large spectral range or a single emission peak [e.g., Wiens *et al.*, 2013] (see Appendix A for detailed methods). Observations use 30 laser shots (or more) to collect spectra at a given point (Table 1). To avoid dust contamination, the first five spectra were always removed before processing the average for quantification. In the following, all major element abundances are measured using a new multivariate calibration (S. M. Clegg *et al.*, Recalibration of the Mars Science Laboratory ChemCam instrument with the expanded geochemical database and a two-step analysis approach, submitted manuscript) and trace element abundances (Cr, Li, Rb, and Sr) are determined from single emissions (Appendix A). Hydrogen will only be discussed semiquantitatively using independent component analysis (ICA, Appendix A) plots because this element has been challenging to quantify with LIBS [Sobron *et al.*, 2012; Schröder *et al.*, 2015]. Given the detection limit of chlorine, sulfur, and phosphorus (typically >5–10%), those elements are rarely detected by ChemCam except in individual minerals of which they are a major constituent. Spectra of all conglomerates were examined for these elements, in case of local enrichments.

The ChemCam laser focuses to a small point, typically ~0.3–0.5 mm in diameter at distances of 2–7 m. With this beam diameter the individual ChemCam spectra do not yield a bulk rock analysis. In the case of large grains, such as phenocrysts derived from igneous rocks, it may provide individual mineral chemistry. In the case of fine-grained sediments, such as mudstones, or aphanitic igneous rocks where grain sizes are small relative to the laser beam, ChemCam provides the bulk chemistry at the scale of the beam. In the intermediate case, data display point-to-point variability in composition, which is related to the natural mineralogical variability in rocks. In such cases, data can be interpreted as due to a mixture of two phases or more [e.g., McCanta *et al.*, 2013; Sautter *et al.*, 2014]. To enable a more statistically representative chemistry, data are usually collected in lines of 5 or 10 points or matrices of 3 × 3, 4 × 4, or 5 × 5 points. These points can then be averaged for calculating the bulk chemistry of a given target or a group of targets of the same nature, such as geological units (see examples in Mangold *et al.* [2015]). The bulk chemistry deduced has a statistical bias related to the number of points acquired on each target (most often <10 in conglomerates, Table 1). As conglomerates contain coarse grains by definition, the chemical variability observed at each target will strongly depend on the number of points as the point-to-point variability is mostly the result of hitting different pure minerals. Note that this methodology is slightly different from Sautter *et al.* [2015] where each phase is identified first from individual points and the average chemistry is calculated by measuring their relative contribution using the RMI images. The latter method is only possible for large clasts with a porphyritic texture.

The APXS instrument provides a measurement of the bulk chemistry of major, minor, and some trace (Cr, Ni, Zn, Br, Ge, Cu, and Pb) elements (Appendix A) [Campbell *et al.*, 2012; Gellert *et al.*, 2013]. APXS provides bulk chemistry over the field of view area (1.5 cm in diameter, when in contact). However, if a rock has phenocrysts, clasts, or grains that are relatively large compared to the area being examined, or other heterogeneities on the scale of the APXS field of view, then results are less likely to represent the bulk rock chemistry. APXS data presented here were acquired on the “as is” surface of the rock target without any cleaning of the surface with the rotating brush called the Dust Removal Tool. Certain elements that are typically present in the dust at higher concentrations than the substrate rock (such as Mg, S, and Cl in this case) will consequently be slightly overestimated in the APXS analyses of dusty targets [Berger *et al.*, 2013]. This is likely the case for the APXS analyses of the Darwin waypoint targets Dragons Teeth, Kerguelen, and Heimdall. The Bardin Bluffs, Ruker, and Jum Jum analyses were relatively dust free compared to the other targets at Darwin. APXS data were not acquired frequently on conglomerates, thus limiting a statistical sampling of this rock type with this instrument.

Table 1. List of ChemCam Observations on Conglomerates^a

	Sol	Target	Type of Conglomerate	Number of Individual Points Analyzed	Number of Shots per Point ^b	Points Removed	Distance (m)
Hummocky plains before Darwin outcrop (sols 1–390)	27	Link	Outcrop in hummocky plains	5	50		2.66
	339	Cosmo	Outcrop in hummocky plains	4	30	F1 and F3	5.40
	343	Frood (1 and 2)	Outcrop in hummocky plains	2 ^b 5	30		3.95 and 4.35
	353	Hector	Outcrop in hummocky plains	9	30		2.35
	353	Howey	Outcrop in hummocky plains	5	30		2.64
	358	Kenwood_River	Float rock in hummocky plains	5	30		3.30
	360	Ham	Outcrop in hummocky plains	9	30		2.76
	363	Labyrinth Lake	Outcrop in hummocky plains	5	30	S4	3.40
	363	Buit Lake	Outcrop in hummocky plains	5	30	S1	4.82
	365	Acme	Outcrop in hummocky plains	9	30		3.80
	370	Gogwanda	Float rock in hummocky plains	9	30	F2 and S4	3.25
	371	Deloro	Outcrop in hummocky plains	5	30		2.66
	372	Terra Nova	Outcrop in hummocky plains	5	30		3.02
	379	Radok	Outcrop in hummocky plains	9	30		2.62
	379	Carrier	Outcrop in hummocky plains	5	30		2.55
	387	Ruker	Pebble of an outcrop in hummocky plains	9	30		2.51
	Darwin outcrop (sol 390–401)	392	Bardin_Bluffs	Darwin outcrop	9	30	
392		Altar_Mountain	Darwin outcrop	9	30		4.93
394		Bardin_Bluffs_Pebble	Darwin outcrop	9	30		2.33
394		Humboldt	Darwin outcrop	9	30		2.34
394		Grainger	Darwin outcrop	5	30	S1	2.40
398		Beacon_Heights	Darwin outcrop	9	30	V5	2.36
398		Camp-Ridge	Darwin outcrop	9	30	V4-8	2.33
399		Platypus_Ridge	Darwin outcrop	10	30		2.59
401		Shackleton	Darwin outcrop	9	30	V1 and V4	2.31
401		Dragons-Teeth	Darwin outcrop	9	30	S1-2	2.42
401		Heimdall	Darwin outcrop	5	30	F2	2.48
Hummocky plains after Darwin outcrop (sols 402–540)	407	Tingey	Outcrop in hummocky plains	5	30	F1 and V3	4.21
	424	Otsego	Outcrop in hummocky plains	5	30	S2 and S3	2.65
	424	Seneca	Float rock in hummocky plains	5	30		2.80
	429	Mount_Marion	Outcrop in hummocky plains	5	30		2.98
	434	CC_BT_0434	Outcrop in hummocky plains	20	30	S1–12	3.12
	514	Harrison	Pebble of an outcrop in hummocky plains	16	30		2.30
	550	Jum Jum	Kylie outcrop	5	30		2.60
Outcrops at Kylie-Kimberley (sols 550–650)	579	Petaluma	Kimberley outcrop	10	30		4.70
	581	Egan	Kimberley outcrop	10	30		5.00
	636	Lambo	Float rock at Kimberley	10	30	S1	2.30
	655	Podunk	Outcrop in hummocky plains	5	30	F2	3.27
Various terrains after Kimberley (sols 650–780)	663	Kinsman	Float rock in hummocky plains	9	30		2.62
	776,778, and 779	Bald Mountain 1, 2, and 3	Outcrop or lag deposit at Pahrump	10, 9, and 9	30		4.80

^aThe column “Points Removed” provides the point number along each raster or matrix for which the laser hit soils (S), or veins (V), or locations for which laser coupling or focus resulted in low-quality quantification (F). Several conglomerate targets were not included because of either low quality of spectra or because they were too far (>5.5 m) for quantification (e.g., targets Goulburn and Red Vine)

^bNote that the first five shots are removed from the quantification in Table 2.

ChemCam data are available on 40 conglomerate targets spread along the rover traverse (Table 1). To provide useful comparisons between the various locations where conglomerates have been analyzed, we have separated these 40 targets into five major groups according to their geographic locations: The first group is defined by the 15 targets (93 points analyzed by the laser) observed before Darwin (sol 0–390). The second group is defined by the 11 targets (80 points analyzed) observed at Darwin (sols 390–400). The third group corresponds to five targets (24 points analyzed) observed after Darwin and before the Dingo Gap (sols 400–540). The fourth group is defined by four targets (34 points analyzed) in the Kylie-Kimberley field area (sols 540–640). The last group is defined by the three targets (41 points analyzed) analyzed between Kimberley and Pahrump Hills (sols 640–780). Ruker (9 points) and Harrison (16 points) are considered separately because they correspond to discrete clasts within conglomerates. These individual clasts are discussed in section 3.4. The composition of each target is calculated by the average of all points analyzed on the target (from 2 to 16 points per target). As heterogeneous targets display variable composition at the scale of the ChemCam laser beam (~0.3–0.5 mm), a mean composition of each conglomerate group is also calculated over a statistically significant number of points (from 24 to 93 points per group, Table 2). APXS data (Table 3) are only available on several of the Darwin outcrop targets (second group), on the Jum Jum target (sol 550, fourth group), and on the Ruker clast analyzed separately. None of these targets were brushed before the analysis. Both APXS and ChemCam data are plotted on the same graphs after having normalized elemental compositions to 100% on a volatile-free basis (Figure 8).

3.2. Major Element Bulk Chemistry

ChemCam average compositions of the five groups of conglomerates are plotted in Figure 8a ratioed over the average Martian crustal composition [from *Taylor and Mc Lennan, 2009*] (calculated using global gamma ray spectrometer measurements and local APXS analyses). All conglomerates analyzed exhibit significant differences relative to the bulk Martian crust, specifically higher alkali and aluminium and lower magnesium contents (see discussion in section 5.1). Here we focus on the differences between the five groups. The first three groups, which include the Darwin outcrops and the hummocky plains before and after Darwin, have similar average composition for all elements. This consistency in composition shows that they belong to the same compositional group, whatever their locations along the traverse. The overall enrichment in Na_2O , K_2O , and Al_2O_3 compared to the crustal average suggests a high feldspar content. The fourth group (Kimberley) displays significant differences relative to the three hummocky plain groups, specifically in that it exhibits an elevated potassium content (reaching 5 times the average Martian crust) and higher iron and magnesium contents. The fifth group is intermediate between the hummocky plains area groups and the Kimberley area group, with enhanced K_2O , though not as high as at Kimberley.

Individual ChemCam targets can be plotted together with APXS data to compare these groups more closely (Figures 8b–8d). ChemCam data in each group display some variability from one target to another, as expected given the fact that the composition of individual targets is obtained from the average of a smaller number of points (down to two points at Cosmo). Despite this statistical limitation, the hummocky plain groups (including Darwin, low K_2O green points in Figure 8) have chemistry that clusters in the same range on the plots (Figure 8). The five APXS observations of Darwin also plot with the low K_2O ChemCam data, with relatively high SiO_2 abundances (50–53%) compared to Mars average crust. Specific individual targets at Darwin and the hummocky plains are alkali rich with K_2O abundances varying from near the crustal average (0.4%) to much higher values (1–2%).

This relatively high potassium content of the hummocky plains conglomerates (first three groups) does not reach the high levels of the Kimberley group (from 2% to almost 4% K_2O , red points in Figure 8). Despite the fact that the Kimberley group is undersampled compared to the others, they all plot in the same region of these diagrams. APXS and ChemCam of the Jum Jum target reveal it to be the most enriched in potassium, and this is interpreted to reflect the bulk composition. Note that the APXS analysis of Jum Jum was not collected on the same surface as the ChemCam data, perhaps explaining differences in chemistry between the two analyses of this target. The conglomerates of the hummocky plains display a correlation between Na_2O and Al_2O_3 , whereas the higher K_2O content of the Kimberley group is not correlated to the same trend in Na_2O and Al_2O_3 . This observation indicates that the high potassium is not related to an increased proportion of the same felsic component present in the conglomerates of the hummocky plains. Some of the Kimberley targets display high iron content, but not all. Although elevated iron does not vary among

Table 2. Major Element Chemistry of Conglomerate Targets Analyzed by ChemCam (Average of All Individual Points on the Same Target, Normalized to 100% of Reported Weight Oxides on a Volatile-Free Basis)^a

	SiO ₂	TiO ₂	Al ₂ O ₃	FeO _T	MgO	CaO	Na ₂ O	K ₂ O
Average Accuracy (RMSEP)	5.2	0.52	3.5	3.8	2.0	2.0	0.7	0.8
<i>Pebbles</i>								
Harrison	53.0	1.05	17.9	12.7	2.5	7.5	3.6	1.8
Ruker_RP_ccam	59.8	1.10	15.5	9.8	2.5	4.9	5.3	1.1
<i>Hummocky Plains (Sol 0–390)</i>								
Link	53.9	1.02	22.2	10.0	1.2	5.6	4.2	1.9
Cosmo	50.2	1.26	21.4	14.7	1.6	4.9	5.3	0.6
Frood	52.6	0.96	17.4	14.1	2.4	6.3	5.4	0.8
Hector	53.1	0.86	15.1	16.1	3.8	6.4	4.1	0.4
Howey	53.0	0.65	18.8	11.4	2.0	8.8	4.9	0.3
Kenwood_River	55.8	1.35	17.5	11.6	1.8	4.6	5.7	1.7
Ham	47.6	1.16	16.9	20.4	2.5	6.3	4.3	0.8
Labyrinth_Lake	49.9	0.98	15.1	21.8	2.1	6.5	3.2	0.4
Buit_Lake	50.8	0.84	20.6	10.3	2.1	8.9	5.0	1.5
Acme	50.9	0.88	17.5	13.9	3.2	7.7	4.9	1.0
Gowganda	55.9	0.63	22.5	6.1	0.7	6.7	6.3	1.2
Deloro	47.4	0.82	15.5	18.5	3.2	10.1	3.9	0.6
Terra_Nova	51.0	1.66	13.3	19.4	2.8	7.5	3.8	0.6
Radok	51.7	0.89	15.8	17.4	2.9	6.6	4.4	0.5
Carryer	50.9	0.87	16.3	16.9	2.6	7.4	4.6	0.4
Average	51.5	0.98	17.5	15.1	2.4	7.1	4.7	0.8
Standard deviation	2.5	0.28	2.6	4.3	0.8	1.5	0.8	0.4
<i>Darwin Outcrop (Sols 390–400)</i>								
Bardin_Bluffs_2	51.2	1.49	15.6	18.2	2.9	5.6	4.5	0.6
Altar_Mountain	48.8	0.86	16.6	20.0	3.3	5.2	4.7	0.6
Bardin_Bluffs2_pebble	52.0	0.81	15.8	17.3	2.3	7.1	4.2	0.4
Humboldt	55.0	0.81	17.5	11.8	2.0	7.1	5.2	0.7
Grainger	50.6	1.48	14.4	21.6	2.5	4.6	4.4	0.4
Camp_Ridge_ccam	50.1	0.93	15.4	17.8	2.9	8.2	4.0	0.7
Beacon_Heights_ccam	54.2	0.85	18.8	10.0	2.3	7.9	5.3	0.7
Platypus_Ridge	52.4	1.06	13.1	17.0	3.7	7.3	4.2	1.3
Dragons_Teeth	52.1	0.84	15.2	13.9	2.5	9.5	4.9	1.2
Heimdall	52.6	0.74	20.2	7.8	1.5	11.3	5.3	0.6
Shackleton	54.0	0.74	15.2	11.5	5.2	8.8	4.0	0.6
Average	52.1	0.96	16.2	15.2	2.8	7.5	4.6	0.7
Standard deviation	1.9	0.27	2.0	4.4	1.0	2.0	0.5	0.3
<i>Hummocky Plains (Sols 400–540)</i>								
Tingey	50.4	0.79	18.9	14.4	2.5	7.0	5.0	1.0
Otsego	53.1	0.81	16.9	15.1	1.5	8.2	4.1	0.3
Seneca	54.7	1.19	10.7	19.8	2.7	6.9	3.6	0.3
Mount_Marion	48.2	1.01	18.2	18.2	1.9	7.0	4.0	1.4
CC_BT_0434a	55.9	0.98	15.9	12.7	2.9	6.7	4.3	0.7
Average	52.4	0.95	16.2	16.0	2.3	7.2	4.2	0.8
Standard deviation	3.1	0.16	3.2	2.9	0.6	0.6	0.5	0.5
<i>Kylie-Kimberley (Sols 540–640)</i>								
JumJum_CCAM	48.9	0.85	16.5	22.1	2.5	2.6	4.5	2.0
Petaluma	45.5	0.85	11.4	25.1	5.7	6.3	2.9	2.3
Egan	42.7	0.93	11.9	29.3	4.3	5.2	2.8	3.0
Lambo	51.3	0.89	15.3	14.0	2.3	9.9	3.3	3.1
Average	47.0	0.88	13.7	22.8	3.7	6.0	3.4	2.6
Standard deviation	3.8	0.04	2.5	6.5	1.6	3.0	0.8	0.5
<i>Post-Kimberley (Sols 640–780)</i>								
Podunk	53.5	0.75	17.2	13.1	2.4	6.1	5.1	1.8
Kinsman	52.3	1.05	15.8	16.9	3.0	4.9	3.7	2.3
Bald_Mountain (all)	48.8	0.89	16.1	19.6	3.4	5.4	4.4	1.4
Average	51.5	0.89	16.4	16.6	2.9	5.5	4.4	1.8
Standard deviation	2.5	0.15	0.8	3.3	0.5	0.6	0.7	0.5

^aFor simplicity, we do not reproduce the error around the average for each target, as these individual locations display a variability linked to the mineralogical variability. The root-mean-square error of prediction (RMSEP) describes the mean accuracy of the measurements.

Table 3. Major Element Chemistry of the Conglomerate at Darwin Outcrop Determined by APXS (Normalized to 100% of Weight Oxides on a Volatile-Free Basis)

	SiO ₂	TiO ₂	Al ₂ O ₃	FeOT	MgO	CaO	Na ₂ O	K ₂ O
	<i>Pebble</i>							
Ruker	57.2	1.45	12.5	10.9	4.7	7.7	4.4	1.0
	<i>Darwin Outcrop (Sols 390–400)</i>							
BardinBluffs2_pebble	53.0	0.57	15.5	16.5	3.4	5.9	4.5	0.6
Bardin_Bluffs_1a_Matrix	51.2	0.76	14.8	18.3	4.0	5.9	4.3	0.6
Dragons_Teeth	50.6	0.94	13.4	15.5	6.7	7.4	4.2	1.2
Kerguelen	51.2	0.97	12.6	15.3	7.4	7.5	3.8	1.3
Heimdall	51.1	1.04	12.1	14.7	8.0	8.3	3.7	1.1
Average	51.4	0.86	13.7	16.1	5.9	7.0	4.1	0.9
Standard deviation	0.9	0.2	1.4	1.4	2.1	1.1	0.3	0.3
	<i>Kylie-Kimberley (Sol 350)</i>							
Jum Jum	49.8	0.87	13.6	16.7	5.3	5.5	4.4	3.8

conglomerates to the degree that high potassium does, a low silicon content is associated with the high iron, providing a trend consistent with a more mafic composition compared to conglomerates of the hummocky plains (Figure 8c).

Lastly, all three targets from the fifth group (in red) plot on the individual diagrams of Figure 8 in intermediate positions between the hummocky plains conglomerates (in green) and the Kimberley group (in orange). Their positions confirm the interpretation made from the average composition in Figure 8a that this group has an intermediate composition. From these results, we propose to classify the chemistry of conglomerates

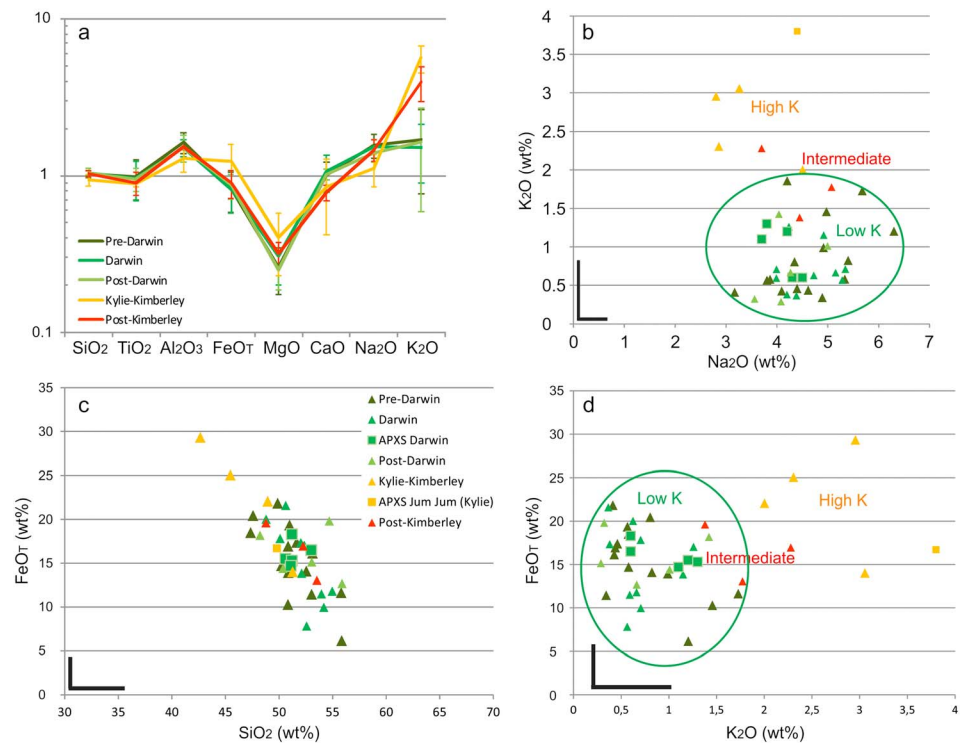


Figure 8. (a) ChemCam major element chemistry of the five groups of conglomerates identified by their geographic locations, as averages of multiple targets. All data ratioed over the mean Martian crust composition from Taylor and Mc Lennan [2009]. The three groups in green are all located in hummocky plains and display similar chemistry. The Kylie-Kimberley group displays high potassium and high iron. (b–d) Plots of the ChemCam chemistry of the individual target average compositions divided into five geographic groups and of the APXS chemistry of Darwin and Jum Jum conglomerates. Individual plots confirm trends in Figure 8a showing especially the high potassium content of the Kylie-Kimberley group. Black rectangles close to the origin indicate the accuracy of ChemCam (RMSEP).

Table 4. Minor Elements and Volatiles Measured by APXS (in Bold) and ChemCam (in Italic) on Common Targets^a

Targets	P ₂ O ₅ (wt %)	SO ₃ (wt %)	Cl (el. %)	Li (ppm)	Br (ppm)	Ni (ppm)	Zn (ppm)	Cr (ppm)	Mn (ppm)	Sr (ppm)
				<i>Pebbles</i>						
Ruker	1.45	4.46	0.85	<i>10</i>	35	36	84	308	1617–1710	<i>360</i>
				<i>Darwin Type</i>						
BardinBluffs2_pebble	0.6	4.48	1.46	<i>16</i>	139	79	246	0	924–1630	<i>250</i>
Dragons_Teeth	0.86	6.08	0.98	<i>21</i>	57	94	731	547	3080–4260	<i>290</i>
Heimdall	0.93	7.78	0.97	<i>17</i>	10	214	782	650	2079–2190	<i>330</i>
				<i>Kimberley Type</i>						
Jum Jum	0.62	4.26	1.35	<i>33^b</i>	90	138	1057	958	1848–2670	<i>310</i>

^aP, S, Cl, Ni, and Zn were below ChemCam detection level on these targets.

^bAverage of five points at Jum Jum with the fifth point having 83 ppm of Li.

into two main compositional types. The consistency in chemistry between the three groups of the hummocky plains enables us to classify them as a single conglomerate type, named the “Darwin type,” by reference to the well-studied outcrop. The potassium-rich conglomerates observed at Kimberley and Kylie are unique and will be kept as a single type, named “Kimberley type.” We interpret the chemistry of the fifth group as representing a mixing between the two types of conglomerates; we therefore do not discuss it in depth.

3.3. Minor Elements and Volatiles

Minor elements and volatiles were not studied exhaustively for all targets. We have chosen to focus on minor and trace elements in targets that were analyzed by both ChemCam and APXS (Table 4). Transition metals (Ni, Zn, Cr, and Mn) do not show specific high or low abundances compared to crustal levels. Jum Jum displays elevated Zn (1057 ppm) in the APXS analysis (ChemCam did not detect Zn above its detection level of 3000 ppm [Lasue et al., 2016]). This elevated Zn concentration at Jum Jum compared to other conglomerates is probably related to the higher Zn detected in the majority of Kimberley sedimentary rocks, not only conglomerates [Thompson et al., 2014; Lasue et al., 2016]. Indeed, 15 Kimberley ChemCam targets exhibited Zn abundance >1% [Lasue et al., 2015, 2016]. In contrast, Jum Jum does not display a significant enrichment in Mn compared to other conglomerates, although Mn is high in the Kimberley sandstones [Thompson et al., 2014; Lanza et al., 2015]. However, many of the Mn enrichments are observed in fracture fills within the Kimberley sandstones suggesting relationships with postdepositional processes [Lanza et al., 2015].

Strontium is detected by ChemCam in the selected targets (Table 4) at a relatively high abundance, approximately 300 ppm; thus, it is of the same order as Earth’s average crustal composition [e.g., Taylor and McLennan, 1995]. The average obscures some larger values observed on individual points, up to 800 ppm in these targets. This is still lower than the sol 27 conglomerate target named Link, which has points reaching 2000 ppm of Sr [Ollila et al., 2014] among the highest values of Sr detected on conglomerates.

Sulfur and chlorine detected by APXS are not particularly high (Table 4, SO₃ < 8%, Cl < 1.5%), and these values are likely an overestimate of the intrinsic content of the rock due to the contamination of dust on the nonbrushed targets (as sulfur and chlorine are relatively high in Martian dust [e.g., Berger et al., 2013]). The Ruker, Bardin Bluffs, and Jum Jum APXS analyses were on relatively dust-free surfaces and indicate ~4% SO₃ and ~1% Cl contents of these rocks. No individual point displays sulfur peaks with ChemCam (detection limit approximately 10% SO₃, in agreement with APXS results). It was not possible to distinguish if this low amount of sulfur was associated with sulfides or sulfates.

Hydrogen has been detected by ChemCam in most Martian rocks, although at low levels. This is also the case for conglomerates, which display low-intensity emission lines with some point-to-point variability. The analysis of targets at Darwin field site indicates that these low hydrogen emissions are not especially correlated with other elements (Figure 9).

Fluorine was detected within conglomerates at several locations (Table 5 and Figure 9e) owing to the observation of a molecular emission of CaF [Forni et al., 2015a]. Fluorine detections are observed as points distributed across a single clast (Harrison), on conglomerates distributed along the rover traverse (Link, Deloro, and Bald Mountain) and in specific outcrops (Lamboos at Kimberley and Platypus Ridge at Darwin). Fluorine detection is not restricted to one conglomerate type. Fluorine abundances of 0.5 to 1.9% were found only in isolated points and would not translate to large average bulk rock compositions, perhaps with the

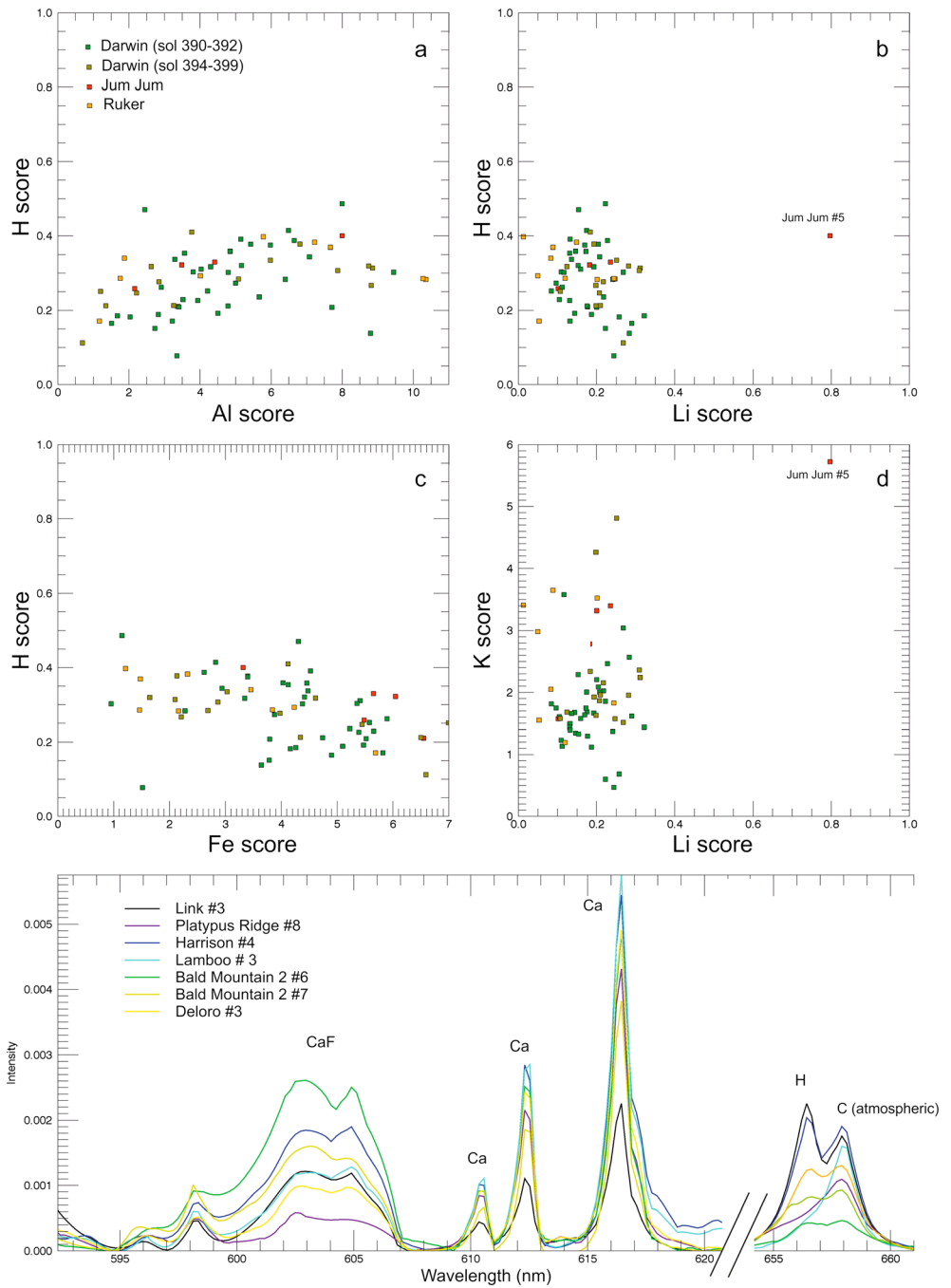


Figure 9. (a–d) Independent component analysis (ICA, Appendix A) plots of targets from Darwin outcrop, Jum Jum, and Ruker targets. Variable hydrogen is observed without significant correlation with any major element. Lithium is only high for the point 5 of Jum Jum, where it is correlated with high potassium content. (e) ChemCam spectra of some of the fluorine-bearing points detected in conglomerates.

exception of Link, where an average content of 1.2% can be estimated because all five points contain fluorine. Fluorine detection is probably not related to a single mineral. Correlations between calcium and fluorine peaks for many targets show that apatite and fluorite are good candidates for these detections. Phosphorus, a structural constituent of apatite, was not detected by ChemCam in these targets (the phosphorus detection limit by LIBS is about 10 wt %). However, the presence of bulk P_2O_5 at approximately 1% in APXS analyses is consistent with apatite playing a role in explaining elevated fluorine. In contrast, at Link, the low intensity of the calcium emission lines suggests the presence of other mineral phases, perhaps micas, as proposed

Table 5. Fluorine Detection in Conglomerates From ChemCam Data^a

Targets	Point Number of Each Target ^b	F (el. %)
<i>Pebbles</i>		
Harrison	4	1.3
Harrison	11	0.5
<i>Hummocky Plains</i>		
Link	1	1.1
Link	2	1.2
Link	3	1.0
Link	4	1.3
Link	5	1.0
Deloro	3	0.7
Mount Marion	1	0.5
<i>Darwin</i>		
Platypus Ridge	8	0.4
<i>Kimberley</i>		
Egan	4	0.5
Lamboos	3	1.2
Podunk	2	0.6
<i>Post-Kimberley</i>		
Bald Mountain	9	0.3
Bald Mountain 2	3	0.4
Bald Mountain 2	6	1.3
Bald Mountain 2	7	1.9
Bald Mountain 2	8	0.5
Bald Mountain 3	2	0.5
Bald Mountain 3	4	0.5
Bald Mountain 3	8	0.3

^aThis table gives the number designation of the point in which fluorine was observed.

^bChemCam LIBS uses multiple observation points on each target.

by Forni *et al.* [2015a]. Note that the presence of hydrogen in varying proportions in these F-bearing points suggests that some of these minerals are also hydrous, which would fit with the presence of both apatite and micas (Figure 9e).

Lithium is detected by ChemCam on Darwin targets at a relatively low proportion with no specific correlation with hydrogen or other elements (Table 4). However, the fifth point of Jum Jum displays a strongly enriched Li peak, at 83 ppm, well above the average (33 ppm) for this target. This also corresponds to a point especially rich in K₂O (Figure 9; see section 3.4 for further details on this point). Overall, volatiles are present in conglomerates but are not present in high abundance. Sulfur, chlorine, fluorine, and phosphorus contents are consistent with the local presence of accessory minerals such as sulfides, fluorite, F apatite, or micas. The presence of low amounts of these minerals does not significantly hinder the identification of the main silicate minerals from individual ChemCam analyses.

3.4. Mineralogy From Individual ChemCam Observations

To derive mineralogy from individual ChemCam observations, we plot four types of points on the same graphs: (i) Eleven individual analyses corresponding to grains that were identified using RMI image analyses are plotted as dark green dots (Figure 10). Below, we demonstrate that only 6 of the 11 points are likely to represent one or two mineralogical phases. (ii) The pebbles Ruker (blue dots) and Harrison (purple dots) that have porphyritic, igneous textures and so are relevant to be included for this analysis. (iii) Jum Jum point 5 was identified as unique based on its chemistry (high K and high Li). (iv) In addition to these targets, we plot all the individual analyses of the Darwin type (green triangles) and of the Kimberley type (orange triangles; “types” are defined in section 3.2) conglomerates. On the plots, some of the points thought to be especially representative of a given mineralogy (i.e., B4 and HW3 for Buit Lake #4 and Howey #3; H13 and H16 for those points 13 and 16 on Harrison; and R1, R3, and R7 for those points on Ruker) are identified for clarity.

Figure 10a plots the molar ratio of Al/Si, sensitive to the identification of aluminosilicates (*Y* axis) against the molar ratio (Fe + Mg)/Si sensitive to the mafic minerals (*X* axis). A number of points plot close to the *Y* axis with most of them plotting close to an Al/Si ratio of 0.5, consistent with andesine plagioclase (An₄₀), or possibly the K-rich feldspathoid leucite. Looking more closely, Buit Lake #4 (B4) is typical of the group of five green dots that plot close to B4, as well as H16 and R9. These are all interpreted as andesine plagioclase based on this plot (Figure 10a). The three other plots (Figures 10b–10d) confirm this interpretation: the same group of points (typified by B4 and H16) plot close to the origin in Figure 10b (K/Si versus (Fe + Mg)/Si) and close to the An₄₀ composition in Figure 10c (Al₂O₃ versus CaO) and in Figure 10d (MgO versus CaO). Leucite is excluded by the low K₂O content (<1%) and low K/Si (which should be 0.7 for leucite) of all these points (Figure 10b). Nepheline is also ruled out by the Al/Si ratio, as the observed values are far too low for this mineral.

Several points plot below the group around B4 in Figure 10a, such as R3, H13, and Jum Jum 5. Their positions are consistent with the presence of alkali feldspars. These points are the most enriched in potassium as seen

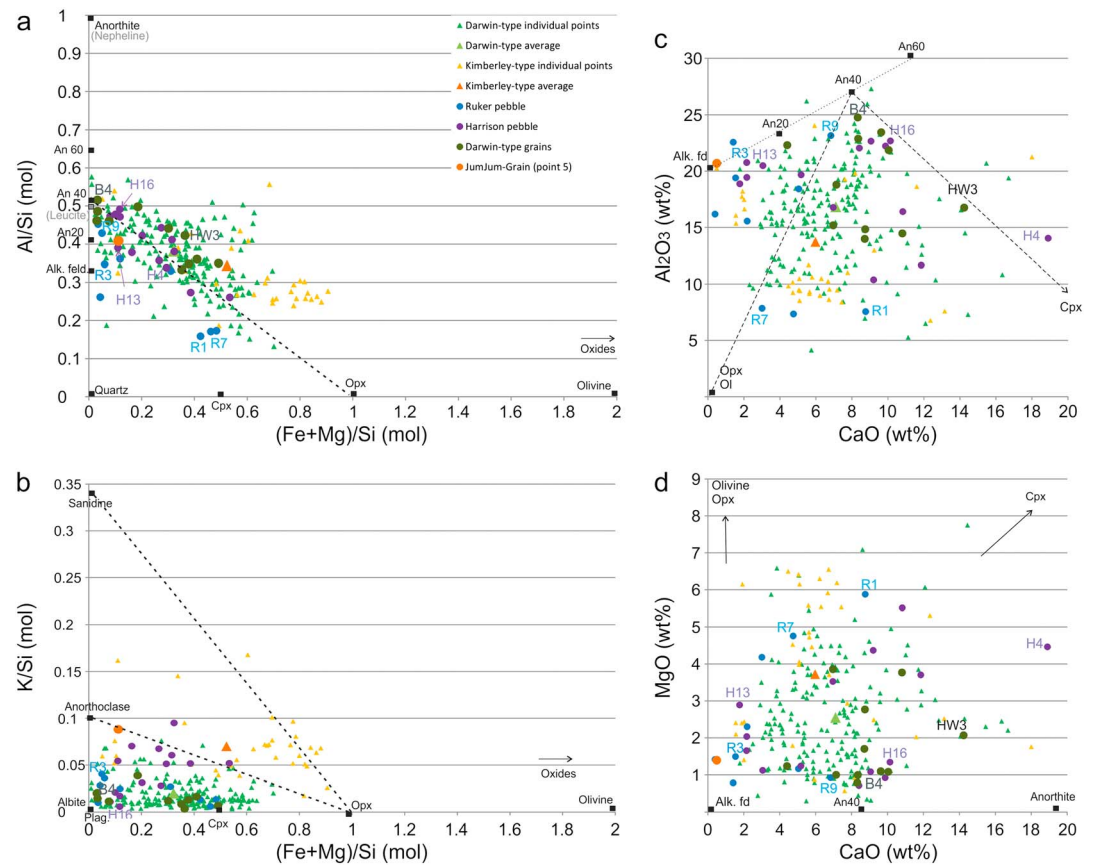


Figure 10. (a–d) Plot of individual ChemCam points of conglomerates (green and orange triangles) and points selected from images and Ruker and Harrison pebbles. Some mineral end-members are plotted (or indicated by arrows). Dotted lines indicate mixing lines between major mineral phases. Black squares are mineral end-members. See text for further explanations.

in Figure 10b, with Jum Jum 5 plotting near the position of anorthoclase. These points also plot at the position expected for alkali feldspars in Figures 10c and 10d, although these figures suggest that the feldspars are mixed with a small amount of mafic material.

Lastly, several data points suggest the presence of ferromagnesian minerals but with much less obvious trends. H4 and HW3 plot toward enhanced CaO and intermediate Al₂O₃ and MgO abundances in Figures 10c and 10d. Their positions on these plots suggest mixing between clinopyroxene and feldspar, and indeed, Figure 10a suggests that the mixing is significant. R1 and R7 in Figure 10a plot toward clinopyroxene as well, and correspond to the lowest Al₂O₃ contents observed, suggesting that the mixing is less pronounced for these two points, but R7 appears to have a better fit with orthopyroxene.

These identifications are consistent with the visual observations. Plagioclase contribution is deduced from this Figure 10 for the points Buit Lake 4, Radok 2, Acme 6, and Heimdall 1, in agreement with their light tones in images (Table 6). This is also the case of Ruker 2 and 9 and Harrison 12 and 14–16, which have been acquired on the light-toned elongated phenocrysts. In contrast, Howey 3, Harrison 4, and Ruker 1, and seven points, were acquired on dark-toned surfaces, in agreement with interpreted LIBS chemistry pointing toward pyroxenes. Overall, these observations suggest that the light-toned phases are dominated by plagioclases, with local alkali feldspars. Mafic minerals seem to be smaller in size and less identifiable by this technique; otherwise we would have observed the mineralogical end-members more clearly.

A broad look at the overall sampling of conglomerates can also be done by investigating the differences between the Darwin type (green triangles) and the Kimberley type (orange triangles). Many points of the Darwin type group are close to B4 and the plagioclase end-member. The rest of the points display a mixing trend predominantly between andesine and orthopyroxene (especially in Figure 10c) or possibly mixing of clinopyroxene with olivine and orthopyroxene. Overall, the mineralogy of Darwin-type conglomerates

Table 6. Individual Points Analyzed for Mineralogical Analysis

Points	Tone on RMI Image	Main Trend
Howey point 3	Dark	CPX + Plagioclase
Labyrinth Lake point 5	Dark	Mixed
Radok point 1	Intermediate	Mixed
Radok point 2	Light	Plagioclase
Buit Lake point 4	Intermediate	Plagioclase
Acme point 6	Light	Plagioclase
Terra Nova point5	Intermediate	Mixed
Deloro point 4	Dark	Mixed
Altar Mountain point 2	Light	Plagioclase + Alk feldspar
Bardin Bluff Pebbles point 2	Intermediate	Mixed
Heimdall point 1	Intermediate	Plagioclase
Ruker points 1 and 7	Dark	Pyroxenes
Ruker points 3, 5, and 8	Light	Alkali feldspar
Ruker points 2 and 9	Light	Plagioclase
Harrison points 12 and 14–16	Light-toned laths	Plagioclase
Harrison point 4	Dark	CPX (predominant)
Jum Jum point 5	Dark	Alkali feldspar

inferred from ChemCam chemical data seems dominated by andesine plagioclase with only a minor contribution of alkali feldspars (Figure 10b).

The Kimberley type plots differently: a group of points typified by Jum Jum 5 plots close to alkali feldspars. This is especially visible in Figure 10c where the six orange triangles can be seen below the Jum Jum 5 orange disk. While Jum Jum 5 plots close to anorthoclase in Figure 10b, these other points display more variability, with three of them displaying higher K_2O content, closer to the sanidine-orthopyroxene mixing line. Besides these Fe-Mg depleted points, another larger group of orange triangles is observed at $(Fe + Mg)/Si$ of 0.7 to 1. This group of points also has low Al_2O_3 and intermediate CaO content. Their position in Figures 10a and 10c suggests a predominance of orthopyroxene, with possible contribution of clinopyroxenes, olivine, or Fe oxides.

3.5. Synthesis and Interpretation of Chemistry and Mineralogy

The chemistry of 40 conglomerate targets analyzed by APXS and ChemCam allows us to distinguish two main groups: the Darwin type consisting of the Darwin outcrop and samples generally exposed across the hummocky plains map unit and a smaller group of conglomerates analyzed in the Kimberley area, located at a higher elevation and possibly a higher stratigraphic position. Further targets acquired after Kimberley, exposed at even higher elevations, suggest a chemical mixing relationship between these two end-members. Both the Darwin and Kimberley conglomerate types have higher aluminium, sodium, and potassium abundance than the bulk Martian crust.

Local measurements of the Darwin type conglomerates show the predominance of plagioclase mineralogy, with the presence of minor alkali feldspars, in agreement with the high Na_2O/K_2O ratio of 5 to 10. The predominance of plagioclase is consistent with the relatively high Sr abundance, because strontium is an element that substitutes easily into the calcium locations of plagioclase [e.g., Drake and Weill, 1975]. The ChemCam chemical analyses (and specifically Al/Si ratios) suggest the absence of feldspathoids such as nepheline or leucite. The predominance of feldspars over ferromagnesian minerals in the individual ChemCam analyses is likely due to the larger grain size compared to the ferromagnesian minerals that may be finer grained and/or present in the matrix. The mafic component seems to be dominated by pyroxenes, predominantly orthopyroxene.

The Kimberley-type conglomerates are distinct from the Darwin-type conglomerates in that they exhibit a much higher potassium and iron content and a much lower Na_2O/K_2O ratios (<2). Individual analyses point toward the presence of alkali feldspars, including anorthoclase and sanidine. An explanation of the potassium-rich component being present as leucite is not supported by the data due to the low Al/Si ratio (<0.5) at these locations. The ChemCam analyses of the ferromagnesian component suggest the presence of olivine or Fe oxides in addition to pyroxenes. Local high lithium may be related to substitution in K feldspar as a consequence of an increase in lithium in late magmatic solutions [Cerny et al., 1985]. Alternatively, it may be related to mobility of fluids in these rocks [Ollila et al., 2014], but hydrogen variations do not seem to have recorded major fluid episodes.

No obvious alteration was observed from ChemCam-derived local mineralogy: Conglomerates can be explained by assemblages of primary igneous minerals. Al/Si ratios do not allow for the presence of kaolinite (with Al/Si = 1). Although smectites have lower Al/Si ratio and could be possible, no correlated enrichment in volatile elements is observed, as would be expected if present in high proportions. However, these observations do not rule out the presence of clay minerals in the matrix between igneous grains. The presence of fluorine supports the presence of either apatite or micas [Forni *et al.*, 2015a, 2015b]. These accessory minerals could account for the variable presence of hydrogen.

As explained in the previous section, the presence of matrix or cement identified in low abundances in the images should not modify the composition significantly. However, we can search for local variations in chemistry to question whether some of these variations could be related to the presence of a fine component. Points with high-intensity hydrogen lines at Link were interpreted to be the result of a hydrated iron-rich, fine-grained component (matrix or cement), as seen from covariations of these two elements in depth profiles within a single observation point (Link #5) [Williams *et al.*, 2013] and in a few outcrops of the hummocky plains [Vasavada *et al.*, 2014]. Such a variation has not been observed systematically among all the conglomerates, neither with iron nor with any other elements (Figure 9). So we suggest that this iron-hydrogen correlation is not typical of all conglomerates nor that the relative matrix proportion matrix is too low to be observed systematically. In conclusion, no systematic chemical variations were attributed to a fine component.

4. Comparison of the Chemistry of Conglomerates With Other Rocks at Gale Crater

4.1. Comparison Between Conglomerates and Finer-Grained Sediments

Most of the sandstones and mudstones analyzed by the rover before sol 800 were deposited by fluvial and lacustrine processes [Grotzinger *et al.*, 2014, 2015], for which the conglomerates are the closest petrographic and likely compositional equivalents to the parent igneous rocks located in the likely source area on the northern wall and rim of Gale Crater. Indeed, coarse clastic sediments contain predominantly grains with little to no alteration, whereas fine-grained sediments, especially mudstones, can include a large proportion of newly formed minerals as a result of chemical alteration of the source rock [Cox and Lowe, 1995]. Looking at differences between conglomerates, sandstones, and mudstones is therefore important for understanding the role of weathering and diagenesis. To achieve this comparison, we have plotted all individual points of the conglomerates (green triangles for Darwin type and orange triangles for Kimberley type) together with five series of points extracted from the Yellowknife Bay formation, Kimberley formation, and Murray formation (Figure 11). Table 7 lists all the targets belonging to these five groups.

The four plots in Figure 11 display the variations in major elements of individual points of all of these targets. We display the actual point-to-point variations in Figure 11 because such a plot highlights the chemical variability related to mineralogical end-members between the conglomerates and other sediments. The differences between the two types of conglomerates are clearly visible on these diagrams. The diagram in Figure 11a highlights the difference in Na₂O/K₂O ratio, with Kimberley having much higher potassium abundance, and the diagram in Figure 11b displays the difference in iron and magnesium contributions. The diagram of K₂O/Al₂O₃ versus TiO₂/Al₂O₃ (Figure 11c) is often used to constrain provenance, because this plot displays the less mobile major elements (Ti, K, and Al) [e.g., McLennan *et al.*, 1993]. This diagram shows variations between alkali feldspars and plagioclase along the Y axis and between mafic and felsic trends on the X axis. A first-order observation from these diagrams is the clear difference between the chemistry of the conglomerates and that of the finer-grained sedimentary rocks. We describe hereafter these differences in more detail.

On the Na₂O versus K₂O plot (Figure 11a), rocks of the Murray and Yellowknife Bay formations plot closer to the Darwin conglomerate type than to the Kimberley conglomerate type but display slightly lower Na₂O/K₂O ratios (Figures 11a and 11d). This lower Na₂O/K₂O ratio could be interpreted as due to a contribution from the potassium-rich Kimberley-type conglomerate with a higher proportion of alkali feldspars. However, the Murray formation composition (Pahrump Hills sediments) is also shifted toward more mafic compositions (low Na₂O and K₂O in Figure 11a and high MgO in Figures 11b and 11d), and the Yellowknife Bay formation composition is shifted even more so. This higher mafic content is also consistent with the higher TiO₂/Al₂O₃ ratio in Figure 11c. Yellowknife Bay sediments thus plot outside the range of almost all conglomerate points in the three panels in Figures 11b–11d. In Figure 11b, the FeO/MgO ratio of conglomerates is relatively high, around 5:1 (visualized by the dotted line). Yet the Yellowknife Bay sediments do not follow the same

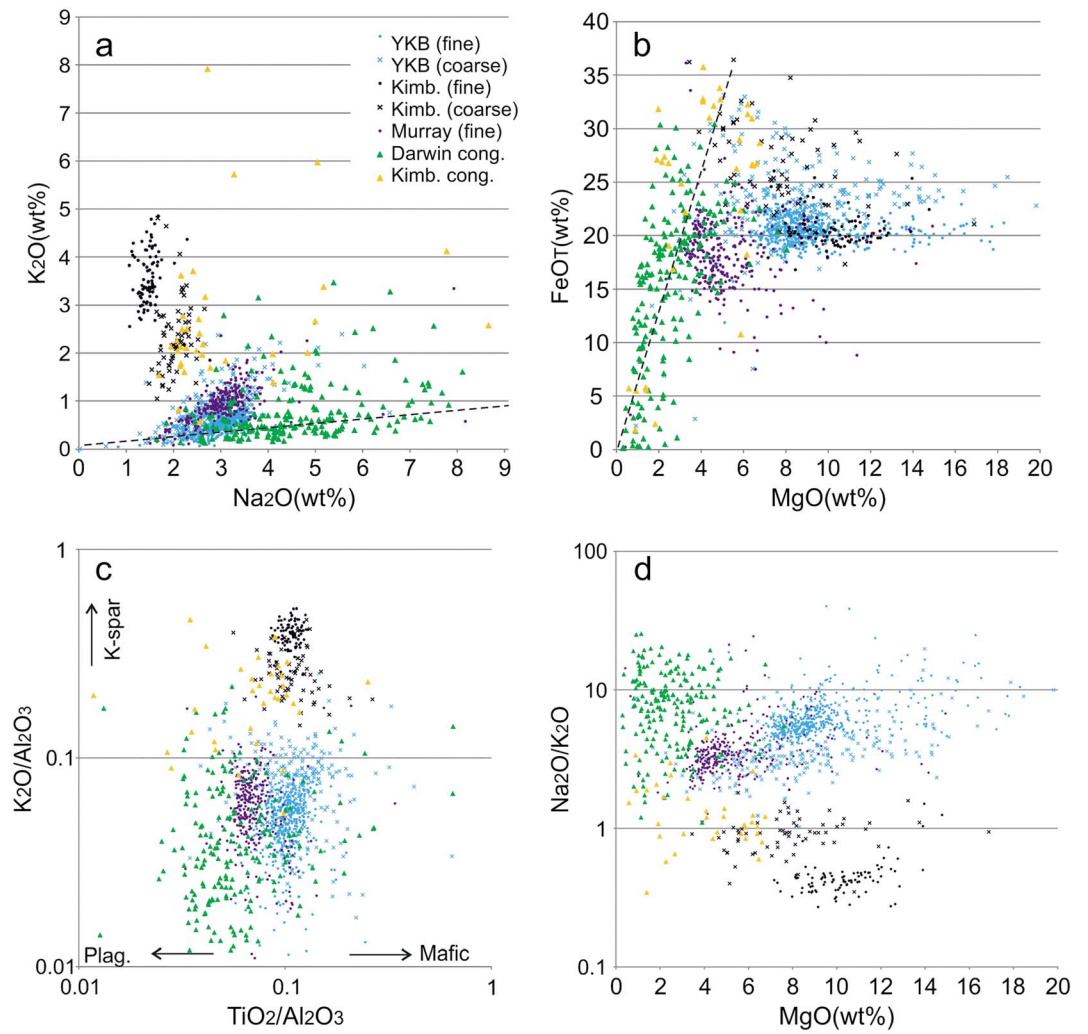


Figure 11. (a–d) Diagram of individual ChemCam points of conglomerates compared to individual points of sandstones and mudstones analyzed by the rover. Individual points aim to show the variability in mineralogy of these rocks. The dotted line in Figure 11a indicates the apparent $\text{Na}_2\text{O}/\text{K}_2\text{O}$ ratio of Darwin-type conglomerates. Yellowknife Bay rocks plot close to the same trend with lower Na_2O abundance. Kimberley conglomerates have a much lower $\text{Na}_2\text{O}/\text{K}_2\text{O}$ ratio, as Kimberley finer-grained sedimentary rocks. The dotted line in Figure 11b illustrates the apparent FeO/MgO ratio of minerals in conglomerates. Both conglomerates display approximately similar FeOT/MgO ratio although with a higher FeOT abundance at Kimberley. This diagram illustrates the iron/magnesium ratio in mafic minerals in these rocks. All of the plotted finer-grained sediments display a higher MgO that is not explainable by an enrichment of the mafic minerals present in conglomerates. Figure 11c shows how the Darwin-type conglomerates plot toward plagioclase compared to Kimberley-type conglomerates. Figure 11d uses the three most variable elements (sodium, potassium, and magnesium) to illustrate the variations in chemistry from all types of sedimentary rocks plotted.

FeO/MgO ratio as the conglomerates, instead having a much higher MgO content. This difference corresponds to a major change in composition between the ferromagnesian contribution of conglomerates and that of both sandstones and mudstones of Yellowknife Bay formation. Indeed, if Yellowknife Bay formation sediments were enriched by the same ferromagnesian minerals present in conglomerates, they should plot along the same axis (on the upper part of the dotted line, more in the discussion section 5.2).

Kimberley formation sediments all plot in the potassium-rich part of the diagrams, in agreement with the interpretation that they have enhanced alkali feldspar contents and possibly other potassium-rich phases. Kimberley coarse-grained sandstones plot in the same range as the Kimberley conglomerates on all diagrams, except perhaps for a slightly higher MgO contribution visible in Figures 11b and 11d. This observation clearly demonstrates a similar provenance for the Kimberley conglomerate type and the coarse-grained

Table 7. List of Targets Used for Comparison Between Conglomerates, Finer-Grained Sediments, and Float Rocks^a

Sedimentary Formation	Member With Number of Analyses	Target Names Used in Diagrams
Yellowknife Bay formation mudstones	Sheepbed member (462 points from sol 125 to 298)	Sheepbed, Beachrock, Belcher, Flaherty, Richardson, Barn2, Rackla, Bonnet Plume, Haig, Hay Creek, Hayhook, Hudson Bay, Quartet, Selwyn, Cape Smith, Kootenay, John Klein, Tutarak, DT_RP5, DT-RP6, Wernecke, Gog, Cumberland, Seward1, Kazan, Fury, Rae, Bylot, Mc Grath, Thelon, Ruth, Cumberland_New, Cumberland_CCAM, Lady_Nye, Duluth, Cumberland3, Sibley, and Mesabi
Yellowknife Bay formation sandstones	Shaler member (225 points from sol 121 to 324)	Stanbridge, Port radium, Rove, Ramah, Michigamme, Wakham Bay, Piling, Chioak, Gogebic, Saglek, Rusty Shale, Reddick Bight, Montaigne, Double_Mer, Ailik Eقالulik, Cartwright, Fabricius Cliff, Steep Rock, Camp Island, and Howells
Kimberley formation coarse-grained sandstones	Square Top member (63 points from sol 576 to sol 591)	Square Top, Square Top 2, Elgee, Top Square Top, and Eastman
Kimberley formation fine-grained sandstones	Dillinger member (89 points from sol 608 to 628)	Wallal, Paperbark, Pentecost, Jarrad, Cow Bore, Kevins Dam, Blinker Hill, and Windjana
Pahrump Hills sediments (Murray formation mudstones and fine-grained sandstones)	All section below Whale Rock (289 points from sol 762 to 799)	Panum, Stovepipe wells, Confidence Hills, Straight Cliffs, Paoha, The Maze, Quartz Spring, White Cliffs, Crowley, Fairyland points, White Cliffs2, Kings Peak, Red Rock Canyon, Hanaupah, Delta, San Rafael Swell, Castle Valley, Ibex Pass, Hayden Peak, Saddle Peak, Goblin Valley, Deadman Pass, Funeral peak, Barstow, San Gabriel, Cajon, Agate Hill, Aztec 2, Crowder, Cima, Sespe, Orocopia, Soleded Pass, Aguerberry Point, and Hackberry Point
Float rocks	Hummocky plains (161 points between sol 0 and 540)	Bird River, Angmaat, Chakonipau, Robin Hood, Fleur de Lys, Stock, Carthew, Dover, Beacon, Ross, Sledgers, Falla, Soldat, Horlick, Becraft, Laurens, Onandanga, Clinton, Sparkle, and Dougalls

^aTargets from the Sheepbed and the Shaler members represent, respectively, Yellowknife Bay mudstones and sandstones [Grotzinger *et al.*, 2014; Anderson *et al.*, 2015; Mangold *et al.*, 2015]. Targets from the Dillinger and Square Top members represent, respectively, Kimberley fine-grained sandstones and coarse-grained sandstones [Treiman *et al.*, 2016; Le Deit *et al.*, 2015]. Targets from Pahrump Hills consist of various fine-grained sandstones to mudstones of the Murray formation [Grotzinger *et al.*, 2015; Blaney *et al.*, 2015]. In data of these targets, only points corresponding to bulk rock have been taken into account (points on soils, veins, etc., were removed).

sandstones of the Kimberley formation. A similar connection is also valid for the fine-grained sandstones but with some modifications because these finer-grained sediments plot apart from both coarse-grained sandstones and conglomerates. Mudstones display a higher potassium content and a lower sodium content that results in a much lower Na₂O/K₂O ratio (<1) than the sandstones. Figure 11b also shows that the FeO/MgO ratio of the Kimberley formation fine-grained sediments is lower on average than Kimberley sandstones. These differences between conglomerates and finer-grained sediments are further discussed in section 5.2.

4.2. Comparison Between Conglomerate Bedrock and Igneous Float Rocks

The conglomerates investigated by Curiosity's instruments are composed of clasts that are predominantly of igneous origin, as shown by their igneous textures. However, the variability in clast/grain texture suggests mixing of several texturally diverse, and presumably compositionally diverse, igneous rock types. A comparison with float rocks that have igneous textures analyzed along the rover traverse is therefore of interest to determine whether these igneous float rocks may simply be clasts liberated from the local conglomeratic outcrops or if they were emplaced by other processes, such as impact-induced ballistic transport, and therefore potentially represent samples from a broader region.

Float rocks chosen for this comparison are those analyzed by ChemCam along the rover traverse, including the target "Jake M" observed by APXS and ChemCam and interpreted as a mugearite, although its texture is not obviously igneous [Stolper *et al.*, 2013]. Float rocks have diverse compositions, including classical basaltic compositions corresponding to dark-toned pebbles and much more felsic compositions corresponding to lighter-toned rocks with frequent coarse or porphyritic textures [Sautter *et al.*, 2014, 2015]. First, individual points of float rocks are plotted with individual points from conglomerates (Figures 12a and 12b) and, second, bulk rock chemistry (averages of all points on a given target) is plotted in Figures 12c and 12d.

Most float rocks plot in the field of the Darwin conglomerates, suggesting that they could be derived from sedimentary outcrops of the hummocky plains (as are the Darwin-type conglomerates). However, a few of them plot apart from most of the individual points (enclosed within black ovals in Figures 12a and 12b).

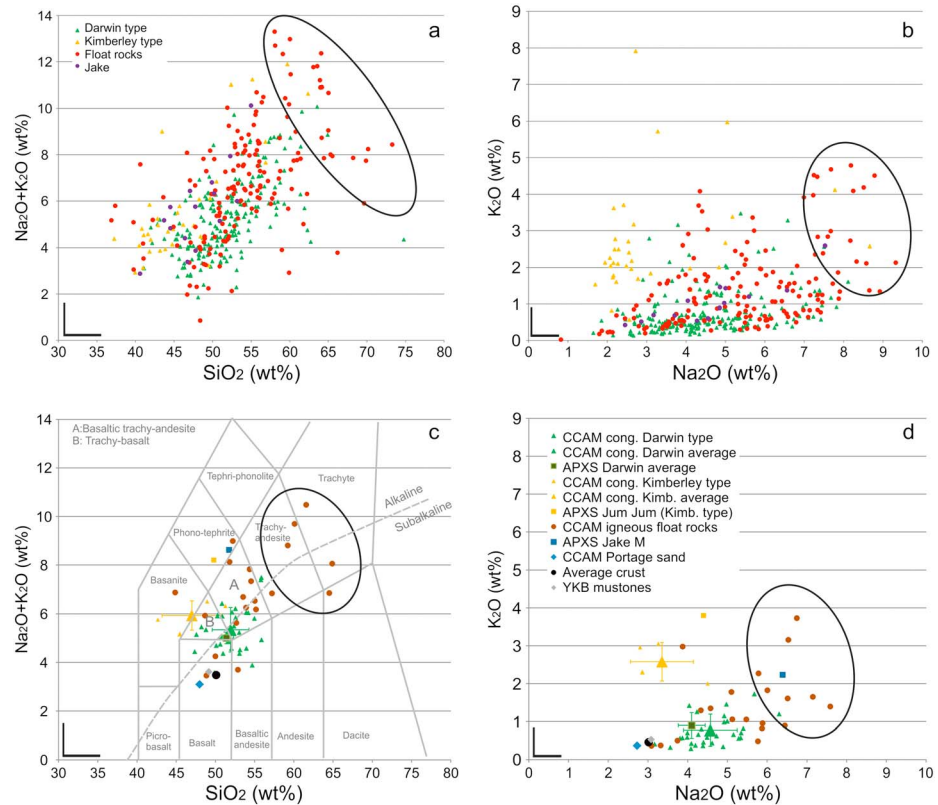


Figure 12. (a and b) Individual points of ChemCam conglomerates compared to float rocks. (c and d) Average composition of ChemCam conglomerates compared to float rocks analyzed by ChemCam and APXS. Black ovals denote float rocks with average composition outside conglomerate compositions.

These points are higher in SiO_2 and in total alkali than most conglomerates. This is even more apparent using bulk rock compositions (Figure 12c) where five points plot inside the dacite, trachyandesite, and trachyte fields. About 65% of the individual points analyzed by ChemCam of these five float rocks are $>60\%$ of SiO_2 , whereas only 6% of the conglomerate individual points are $>60\%$ SiO_2 . Still 28% of the points of the five float rocks are above 65% of SiO_2 , whereas only 1% of points of conglomerates are above that value. Given these differences, the source rocks of these float rocks may have contributed to clasts in the conglomerates only at a low level such that their extreme compositions are diluted, or these five float rocks may have been emplaced by other processes (such as impact processes).

Kimberley type conglomerates have similar total alkali content but with higher potassium contents than Darwin conglomerates, as seen in Figures 12b and 12d. Relatively few individual points of the float rocks plot within the same fields as the Kimberley conglomerates. The bulk rock compositions of the Kimberley-type conglomerates are quite different from that of most float rocks; however, one point does plot close to Kimberley on the Na_2O versus K_2O diagram (Figure 12d). This float target was named Laurens (sol 435) and is the only one to have chemistry close to that of the Kimberley type. The float rocks selected in these diagrams have all been acquired before sol 540, and not much data on float rocks were acquired during the Kimberley campaign (sols 540–660), explaining a possible gap in the data. However, the low number of float rocks consistent with the Kimberley conglomerate type also suggests that the latter were accumulated from less extensive source rocks on Gale Crater’s rim.

Jake M has been interpreted as a nepheline-normative mugearite with a high $\text{Na}_2\text{O}/\text{K}_2\text{O}$ ratio of 3 [Stolper *et al.*, 2013]. Although it plots close to the range of the Darwin-type conglomerates in the Na_2O versus K_2O plot (see APXS data in Figure 12), it plots well above both conglomerate types in the TAS diagram, in agreement with a potential feldspathoid-bearing composition. However, no feldspathoid has been identified in the ChemCam data of individual conglomerate points (see section 3.4). Rather, these data suggest that the Darwin-type conglomerates are best represented as mainly classical subalkaline composition dominated

by plagioclase feldspars. A strong contribution of Jake M type rocks as a source for Darwin conglomerates is therefore unlikely, although a small contribution is possible. A significant contribution of Jake M type to the Kimberley type is even less likely given the opposite trend in the $\text{Na}_2\text{O}/\text{K}_2\text{O}$ ratio.

5. Discussion

5.1. Conglomerate Composition as a Proxy of the Average Igneous Crust Composition at Gale Crater

Conglomerates provide information about igneous parent rocks at the source of the transported sediments, i.e., from the north rim of Gale Crater. Gale Crater's walls reach 3–4 km in height, suggesting exhumation of crustal rocks from that depth. The crater diameter (~160 km) implies that rocks from depths of ~10 km could have been excavated from the crust and be present in the ejecta [e.g., *Melosh*, 1989]. As the Peace Vallis watershed incised both the northern crater rim and the ejecta beyond [*Palucis et al.*, 2014], conglomerates likely represent a mixture of rock samples representative of this ~10 km thick section of crust. It should be noted that this sampling represents a unique location of the crust that we may not be able to extrapolate to the whole Martian crust in general. A growing volume of literature is related to the nature and composition of the early Martian crust that we summarize briefly here to provide material for the discussion on the representativeness of Gale Crater crustal rocks.

Analysis of data from orbiting infrared spectrometers suggests that Mars consists of a basaltic crust dominated by plagioclase, pyroxene, and olivine [*Bandfield et al.*, 2004; *Mustard et al.*, 2005]. These data show a predominance of high-calcium pyroxenes and olivine in Hesperian and Amazonian volcanic plains while low-calcium pyroxenes are found in much higher abundance in the Noachian crust [*Mustard et al.*, 2005; *Poulet et al.*, 2009; *Mangold et al.*, 2010; *Ody et al.*, 2012]. Ancient crustal outcrops are locally ultramafic in regions such as Nili Fossae [*Hamilton and Christensen*, 2005], although these rocks have since been interpreted as ejected from the mantle by the Isidis impact [*Mustard et al.*, 2007]. However, these orbital techniques are not well adapted to the detection of felsic minerals such as alkali feldspars, which are only identifiable by thermal infrared spectrometry (such as the thermal infrared spectrometer, TES) at abundances >10% [*Bandfield et al.*, 2004]. The large pixel size (3 km × 3 km) for TES also limits the detection of these minerals that are not expected to be present at such high levels on average.

So the relatively high abundances of mafic minerals that have been reported are potentially influenced by a bias in the techniques used. In addition, orbital spectrometers study the surface and are biased by the large amount of eolian sediments that may not be locally derived, as well as the presence of dust, which has a generally basaltic composition and mineralogy and can mask the spectral signal of the underlying rock. An excellent example of this is at Yellowknife Bay, the first location that Curiosity drove to for more in-depth studies utilizing the full instrument payload. Detailed compositional and mineralogical data were obtained from two drill holes in the Sheepbed mudstone and indicated the presence of ~20% smectite clay minerals in this region [*Vaniman et al.*, 2014]. CRISM/OMEGA spectral data did not detect these clay minerals, which are interpreted to be present throughout this relatively high thermal inertia unit, exposed over at least 4 km² [*Grotzinger et al.*, 2014]. The presence of effusive volcanic rocks at the surface versus intrusive bodies, which are more likely to be the source of some of the more alkaline and potassic igneous rocks and were never exhumed due to limited erosion, may also explain the relative paucity of feldspar and felsic compositions detected from orbit. Noachian highlands are locally covered by intercrater plains of volcanic or sedimentary origin as well as more recent soils and do not display higher alkali from gamma ray spectrometer data [e.g., *Taylor et al.*, 2010]. Yet local outcrops of more evolved rocks have recently been proposed, such as anorthosites [*Carter and Poulet*, 2013], granitoids [*Wray et al.*, 2013], or dacite [*Christensen et al.*, 2005]. Some of these outcrops are located in the central peaks of craters and around large impact craters (e.g., Hellas) suggesting the possibility of significant differences between the composition of the crust at depth compared to its relatively mafic surface.

Most Martian meteorites (known as SNC for Shergottites, Nakhilites, Chassignites) have alkali-poor basaltic compositions [e.g., *McSween et al.*, 2003, 2009]. But most represent effusive magmatism or cumulates that postdated the formation of the ancient crust. One exception is the recently found feldspar-rich Noachian meteorite breccia NWA 7034 (paired with meteorites NWA 7533 and NWA 7475 [*Agee et al.*, 2013; *Humayun et al.*, 2013; *Wittmann et al.*, 2015]). The overall chemical composition of this meteorite shows alkali-rich lithologies, with an average of ~5% of alkali feldspars [*Agee et al.*, 2013; *Humayun et al.*, 2013]. In addition, the gravity signatures observed over the southern hemisphere led to the conclusion that less

dense rocks (such as felsic rocks) may represent a significant component of the ancient crust [Baratoux *et al.*, 2014]. In this context, the recognition of alkali-rich, leucocratic rocks by Curiosity adds to a growing body of evidence that the composition of primary minerals of the ancient crust into which the north rim of Gale Crater was formed is different from the overall basaltic-dominated crust observed up to now by surface instruments [Sautter *et al.*, 2014, 2015; Schmidt *et al.*, 2014; Cousin *et al.*, 2015]. Relatively felsic rocks at Gale Crater may come from deeper regions of the crust than the mafic components observed from orbital data at the surface. Results from some of these rocks are used in the comparison displayed in section 5.2.

The igneous float rocks have been interpreted to indicate the presence of intrusive bodies or exposures of primitive crust with a variety of compositions [Sautter *et al.*, 2015]. The ChemCam targeting of float rocks was often motivated by the presence of unusual (relative to their surroundings) texture or tone, and thus, they are not likely to be statistically representative of the diversity present in the hummocky plains, i.e., many classic basaltic float rocks were not analyzed although they may be more frequent than light-toned rocks. Thus, the sampling of float rocks might not be representative of the average composition of all igneous rocks present in Gale. As a consequence, it is impossible to derive the average composition of the Noachian crust at Gale Crater from the biased distribution of float rock composition. In contrast, the conglomerates observed along the rover traverse display a variety of grains with contributions of various rocks distributed along Gale Crater northern and western rim, and ejecta. As coarse clastic sediments represent mainly unaltered source rock [Cox and Lowe, 1995], we propose that the average conglomerate composition is representative of the crust at Gale Crater. We propose to use the composition of the Darwin type as an average representative of the terrains analyzed by the rover. In our judgment, the Kimberley type likely represents an enrichment that is more local and less representative, a conclusion supported by the far lower number of float rocks (only the Laurens target) plotting inside the range of Kimberley-type conglomerate compositions. This last point should nevertheless be revisited after a better understanding of the potassic rocks [e.g., Treiman *et al.*, 2016; Le Deit *et al.*, 2015; Thompson *et al.*, 2014] and additional information along the rover traverse.

The average composition of the Darwin type of conglomerates is more Si and alkali rich than the average Martian crust. Apart from the Gale rocks, only those of the Columbia Hills at Gusev, presumed to be Noachian in age, display higher alkali content than the average crust, but with relatively low SiO₂ content [e.g., McSween *et al.*, 2006]. All post-Noachian compositional data consist of basaltic rocks of which those from the Gusev plains are typical Hesperian-aged examples. Accordingly, whereas typical Hesperian and younger rocks plot at lower SiO₂ and lower total alkalis abundances relative to the average crust (Figure 13), Darwin-type conglomerates plot at higher values than the average crust, but closer to it compared to more felsic components of float rocks. Indeed, while felsic, alkali-rich clasts are prevalent, the conglomerates do not consist solely of andesite/trachyte rocks but contain basaltic material as well. As the average Mars crust corresponds to a balance between crust composition of various ages, conglomerates provide a possible representative composition for a Noachian component of the crust (Figure 13). Further discussions on the magmatic origin of the felsic component of the crust can be found in Sautter *et al.* [2015].

A last point linked to the understanding of the Noachian crust is the relative contribution of a primary crust suggested to have formed within 50 Myr after accretion following crystallization of a magma ocean [e.g., Elkins-Tanton *et al.*, 2005]. This process led to an anorthosite crust on the moon. While the composition of a Mars magma ocean may have led to a different suite of minerals, it should be mentioned that the mineralogical diversity observed in conglomerates does not support the presence of pure anorthite or any high-Ca plagioclase. Our observations favor a more sodic plagioclase such as andesine that may not be explained by magma ocean crystallization. CheMin data on fine-grained sediments at Yellowknife Bay also determined that the plagioclase component is mostly andesine [Vaniman *et al.*, 2014].

5.2. Compositional Differences Between Conglomerates and Finer-Grained Sedimentary Rocks

A particularly interesting characteristic of the Gale Crater sedimentary rocks is the presence of fluvial sediments of different compositions. Fluvial sediments were encountered at Yellowknife Bay, especially in the Shaler member where cross-bedding and grain size indicated dynamic flows. The Sheepbed mudstone member, which lies at the base of the Yellowknife Bay formation, was interpreted as lacustrine [Grotzinger *et al.*, 2014]. In the Kimberley formation, the sandstones from the Square Top member display coarse grains, whereas siltstones and fine-grained sandstones compose the Dillinger member, lying immediately above Square Top [Grotzinger *et al.*, 2015; Le Deit *et al.*, 2015]. The Pahrump Hills member of the Murray formation is

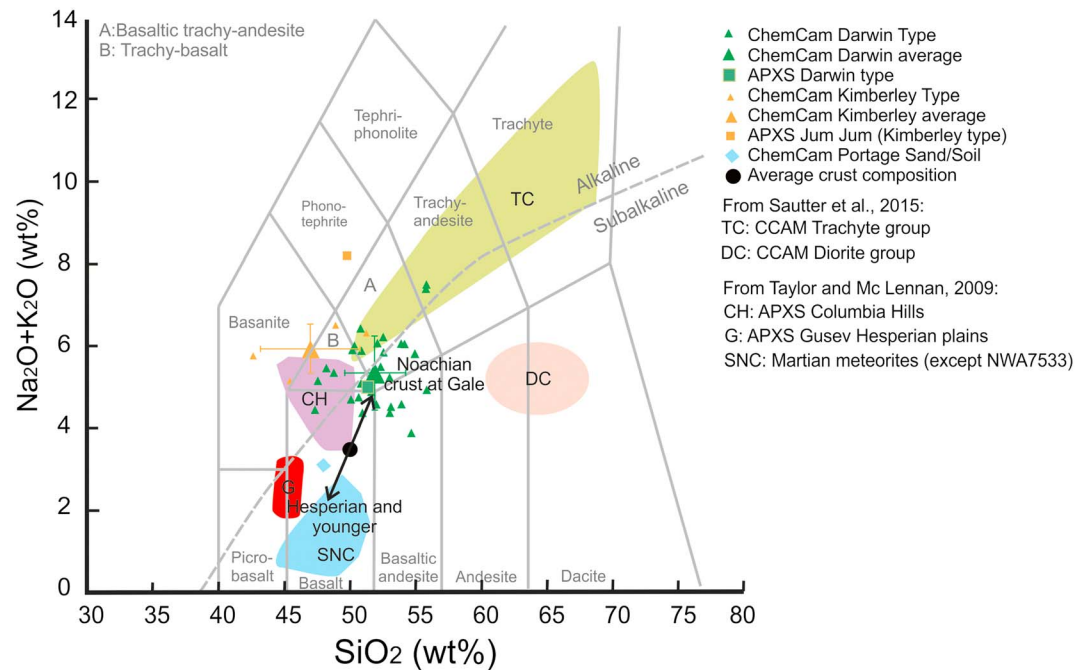


Figure 13. TAS diagram of all conglomerate data compared to some previously published data for the Martian crust. Conglomerate average composition plots in the other direction than the Hesperian plain composition relative to the average Martian crust. The arrows suggest that the Noachian rocks at Gale Crater may be representative of a more felsic composition that contrasts with the common basaltic composition predominant in younger rocks.

the highest point in elevation along the traverse up to that point in the mission and is composed of mudstones and fine-grained sandstones with various facies but with relatively homogeneous composition [Blaney *et al.*, 2015; Thompson *et al.*, 2015].

On Earth, it has been shown that fine grains are sometimes sourced from rocks farther away than coarse grains, as observed using minor elements [e.g., McLennan *et al.*, 1990]. For this work, we do not have the analyses of trace elements (such as Nd) that would be necessary to assess this possibility, but the observation that all these sediments could have formed within the same depositional sequence eroded from the Gale Crater rim (as demonstrated in Grotzinger *et al.* [2015]) is a basic assumption that enables us to compare fine-grained sediments with conglomerates. The source rocks for a conglomerate include all rock types in the watershed that are eroded and contribute to the conglomerate. When the watershed changes or new rocks are exposed for erosion, the source rock composition may shift due to input from new and potentially distinctive rock types. Differences between coarse-grained gravels and fine-grained sediments from the same sources should be limited to compositional changes related to mineral sorting of different grain sizes or different diagenetic environments during or after deposition. More significant compositional differences between coarse-grained and fine-grained sedimentary rocks in the basin indicate that there may be a distinctive watershed or eolian or volcanic source component contributing to the composition of the fine-grained sedimentary rocks that bypasses the conglomerates spatially or temporally.

Here we use two diagrams as in Figure 10 but we have overlain the average values of each unit studied on the point distribution (Table 8) and included arrows to suggest variations required to shift from the conglomerate compositions to that of coarse-grained sandstones, fine-grained sandstones, and mudstones (Figure 14). The fine-grained sediments of the Pahrump Hills member (Murray formation) have a composition close to that of conglomerates with slightly higher MgO contents. This is verified on both plots in Figure 14. The average Pahrump Hills composition may reflect mixing of the two sources that contributed to the two conglomerate types (it plots between the two average conglomerate compositions on both diagrams). This is consistent with the fact that post-Kimberley conglomerates sampled before and nearby Pahrump Hills sediments (red line and points in Figure 8) are also intermediate in composition. Pahrump Hills sediments are consistent with a similar source rock to that of conglomerates with only minor modifications in major elements (slightly higher MgO abundance).

Table 8. Average Composition of Sedimentary Units Analyzed by ChemCam^a

Unit	Number of Points		SiO ₂	TiO ₂	Al ₂ O ₃	FeO _T	MgO	CaO	Na ₂ O	K ₂ O
	Number of Points	Analyzed								
Sheepbed (Yellowknife Bay formation mudstones)	462	462	49.2	1.05	10.5	20.5	9.3	5.8	3.1	0.5
Shaler (Yellowknife Bay formation sandstones)	225	225	46.9	1.20	10.6	23.1	8.5	6.0	2.8	0.9
Dillinger (Kimberley formation fine-grained sandstones)	130	130	48.8	0.94	8.9	20.6	10.3	5.5	1.5	3.5
Square Top (Kimberley formation coarse-grained sandstones)	114	114	45.1	0.97	9.1	26.5	7.7	6.1	2.0	2.4
Pahrump Hills (Murray formation mudstones and fine-grained sandstones)	343	343	51.8	1.04	15.0	18.2	5.3	4.7	3.1	0.9
Darwin-type conglomerates	197	197	51.9	0.97	16.9	15.2	2.5	7.2	4.6	0.8
Kimberley-type conglomerates	34	34	47.0	0.88	13.7	22.8	3.7	6.0	3.4	2.6

^aData compiled using the new calibration that displays minor variation compared to previous studies. Note that among these variations, an important change is the better estimation of MgO compared to previous database that was inconsistent below 4% [Mangold et al., 2015]. Differences with previous works also come from the fact that all abundances are normalized to 100% on a volatile-free basis.

Compared to both conglomerate types, Yellowknife Bay sandstones and mudstones display a stronger shift toward higher MgO abundances and a generally more mafic composition (blue arrow in Figures 14a and 14b). This shift does not follow the FeO/MgO ratio suggested by the individual conglomerate points (Figure 14a). In contrast, Yellowknife Bay formation sandstones and mudstones are very similar in composition, arguing that their sediments were deposited from a common source [Anderson et al., 2015; Mangold et al., 2015]. Nevertheless, the factor of 2 higher Na₂O/K₂O ratio of Yellowknife Bay formation mudstones compared to sandstones (red arrow in Figure 14b) suggests a lower proportion of alkali feldspars than sandstones.

At Kimberley, the common origin of the Kimberley conglomerate type and finer-grained sediments of the Kimberley formation is demonstrated by the low Na₂O/K₂O ratio of all sediments, but there is a shift toward higher MgO content (black arrow) for finer-grained materials, similar to that observed for Yellowknife Bay sediments. Here too, this shift does not follow the FeO/MgO ratio suggested by the conglomerate individual points (Figure 14a). Sanidine is suggested by Figure 10, in agreement with the identification of sanidine by CheMin in the Kimberley finer-grained sandstones (Windjana drill target) [Treiman et al., 2016]. However, the finest-grain rocks have a lower Na₂O/K₂O ratio than the sandstones (orange arrow in Figure 14b), suggesting a different process than at Yellowknife Bay where the trend was in the opposite direction.

We identified three processes that are able to explain compositional differences between conglomerates and finer-grained sediments: (A) The difference may be due to a stronger physical weathering, including mechanical sorting or mineral abrasion during sediment transport [e.g., Fedo et al., 2015]. (B) The difference may be related to a stronger chemical alteration (in the source area or at the site of deposition), or diagenesis at the site of deposition for the finer-grained lithologies, including fluid circulation and postdepositional leaching or addition

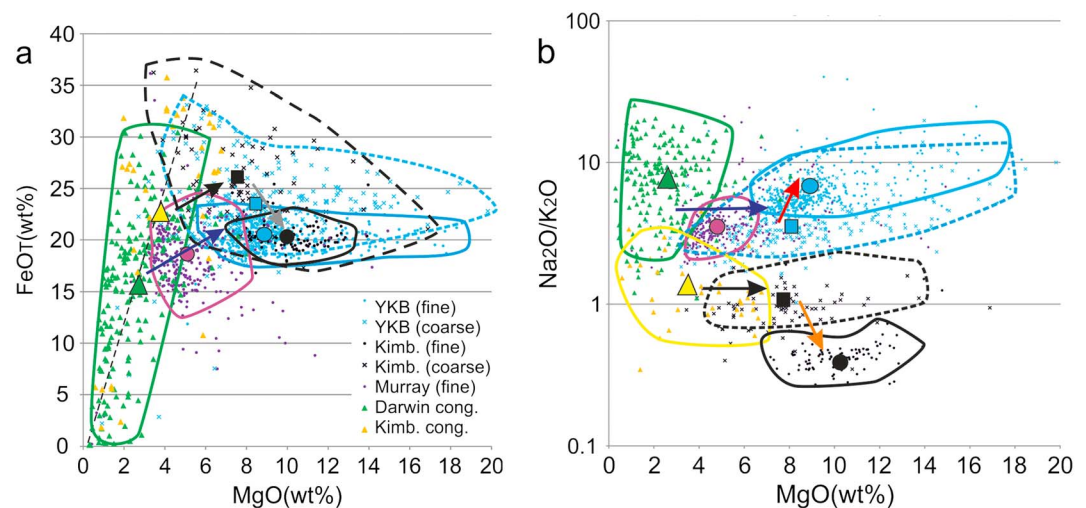


Figure 14. Same as Figures 11a and 11d with interpretative sketch and average of each group superimposed. Arrows indicate possible chemical modifications assuming that the conglomerates were formed by the same processes than sandstones and mudstones but with less modification from the original source rocks.

of cement [e.g., Cox and Lowe, 1995]. (C) The difference may be related to a shift of provenance, like a drainage reorganization and/or in the type of material eroded, or a contamination by other material, like eolian sand or ash, or material from Gale Crater central peak.

Among the differences observed, the increase in MgO from conglomerates to finer-grained material is observed for all sediments. Mechanical sorting can segregate some minerals relative to others due to initial differences in grain density or size (process A). This can lead to a higher content of mafic phases such as olivine [e.g., Mangold et al., 2011; Fedo et al., 2015]. However, the marked difference in FeO/MgO ratios exhibited by the finer sedimentary rocks compared to the conglomerates (from high to low) suggests that this cannot by itself explain the observed trend; a higher Fe content would also be expected. In addition, Chemcam mineralogical identifications indicate the presence of pyroxenes (see section 3.4) although sorting of pyroxenes is unlikely here, because CaO is not significantly higher in sandstones relative to conglomerates. Enrichment by a nearly pure Mg phase such as enstatite or forsterite could explain the trend to high Mg and low Fe in the conglomerates, but ChemCam mineralogical analyses did not indicate the presence of such phases (Figure 10d). The lower Fe content of mudstones versus sandstones (grey arrow in Figure 14a) appears to also rule against this process at finer grain sizes. So sorting effects may have increased the amount of ferromagnesian minerals [see also Siebach et al., 2015] but are unlikely to be responsible for all variations observed by ChemCam.

The higher MgO could be related to diagenetic fluids (process B), as noticed in the course of ChemCam and APXS analyses of the Pahrump Hills member using analyses of diagenetic features such as dendritic concretions and raised ridges [Nachon et al., 2015; Blaney et al., 2015; Thompson et al., 2015]. Mg-rich fluids were also involved in the infilling cement stratigraphy of diagenetic raised ridges in the Sheepbed mudstone (Yellowknife Bay formation) [Léveillé et al., 2014], and the relative MgO variations between the various sandstones of Yellowknife Bay formation were interpreted as variations due to the presence of Mg-bearing cements and their local dissolution [Mangold et al., 2015]. Our observations presented in Figure 14 are consistent with such interpretations, given that all individual points in fine-grained sediments display a higher MgO proportion than the conglomerates with a trend showing individual points stretching horizontally at $\text{MgO} > 10\%$.

Lastly, a possible alternative explanation would be a contamination by dust/sand (process C), especially if those mafic sediments include a source not related to the Gale Crater rim as is likely the case for the conglomerates. A mixing between two different materials (ancient crust and mafic sand) could result in a composition close to the average crust (as the case for Yellowknife Bay [McLennan et al., 2014]) and could explain the different FeO/MgO ratio as well as the more mafic composition of the finer-grained sediments, as plotted on the provenance diagram (Figure 10c).

A second important observation is the variations in potassium content. Sorting (process A) can remove the presumed coarsest minerals (i.e., alkali feldspars) from the phases transported into fine-grained deposits [e.g., Fedo et al., 2015]. Such a sorting effect could contribute to the higher $\text{Na}_2\text{O}/\text{K}_2\text{O}$ ratio between sandstones and mudstones at Yellowknife Bay, but not at Kimberley where the trend is opposite, with a higher potassium content. Hence, the higher potassium content could only derive from a physical sorting if the sorted phase is a fine-grained texture for which clay or micas are better candidate than alkali feldspars. ChemCam observations of fluorine in these sediments may be linked to micaceous phases [Forni et al., 2015b]. CheMin data indicate that illite might be present, although collapsed nontronite or smectite probably provide a better fit of the observed diffraction pattern [Treiman et al., 2016]. Physical sorting of finer-grained material enriched in potassium has been observed on Earth in turbidite sequences due to illite [Kiminami and Fujii, 2007]. The enrichment of $\sim 1\%$ of K_2O between conglomerates/sandstones and finer-grained sandstones of Kimberley sediments (Table 8) would require $\sim 14\%$ illite (as illite contains 7.3% of K_2O) or $\sim 10\%$ of a K-bearing mica such as muscovite or biotite. However, CheMin data do not support such a content of crystallized phases [Treiman et al., 2016]. Nevertheless, amorphous phases (estimated as 25% in the Windjana drill target [Treiman et al., 2016]) could account for some of the K-bearing phases, e.g., poorly crystallized clay minerals, as calculated by Dehouck et al. [2014] and Dehouck and McLennan [2015].

Alternatively, fluid circulation (process B) or a provenance shift (process C) could explain the higher K content of fines. Even if potassium feldspar can form by diagenesis, the preservation of olivine and of amorphous material in Kimberley sediments argues against an extensive diagenetic process for this enrichment [Treiman et al., 2016]. In contrast, we cannot exclude the possibility that part of the finer-grained deposits would derive from a source richer in K feldspars (and/or possibly K-bearing hydrous silicates) than the

Kimberley-type conglomerates, including K-rich air fall deposits (i.e., ash deposits) [e.g., *Leberkmo and Campbell, 1969*]. In the latter case, the initial assumption of K feldspars being present as coarse grains would then be wrong.

In summary, the composition of fine-grained sediments at Pahrump Hills (Murray formation) is consistent with a source similar to a mixing of the two types of conglomerates defined in our study with only small modifications, such as a slight enrichment in MgO. Mg-rich diagenetic features have been observed at Pahrump Hills [*Nachon et al., 2015*] and may have contributed to this overall enrichment. For the Yellowknife Bay formation, the strong differences between the compositions of conglomerates and the finer-grained sediments cannot be explained by a single process. If these sediments are derived from the same source as the conglomerates, both physical sorting and Mg enrichment from circulating fluids (and/or Mg cements) may explain the systematic shift toward higher Mg compositions. Mixing with more mafic sources cannot be excluded, although it is not necessary to explain the observed compositions. At Kimberley, the specific high-K content of the Kimberley-type conglomerates and finer-grained sediments is consistent with a similar source for both, assuming some sorting of potassium-bearing clay/mica/poorly crystalline phases into the finer-grained material. However, a source rock enriched in potassium feldspars or a contamination by potassium-rich air fall deposits is viable alternative to explain the higher K content of the finer-grained sediments.

6. Conclusion

The Curiosity rover has analyzed various sedimentary rocks at Gale Crater, among which fluvial and lacustrine rocks are predominant [*Grotzinger et al., 2014, 2015*]. Conglomerates correspond both to the coarsest sedimentary rocks analyzed and the least modified by alteration, enabling us to link their composition to that of source rocks on the Gale Crater rims. In this study, we reported the results of six conglomerate targets analyzed by APXS and 40 conglomerate targets analyzed by ChemCam. The bulk chemistry derived by both instruments suggests two distinct end-members for the conglomerate compositions. The first group (Darwin type) is typical of conglomerates analyzed before sol 540; it has a relatively more felsic alkali-rich composition compared to the Mars average crust and to previously studied basaltic regions, with a high $\text{Na}_2\text{O}/\text{K}_2\text{O} > 5$. Second, the Kimberley type is typical of conglomerates analyzed between sols 540 and 670 in the vicinity of the Kimberley and Kylie waypoints; it has an alkali-rich potassic composition with $\text{Na}_2\text{O}/\text{K}_2\text{O} < 2$. The variety of chemistry and igneous textures (when identifiable) of individual clasts suggests that each conglomerate type is a mixing of multiple source rocks. ChemCam analyses of individual grains show that plagioclase (andesine) and a mixing of pyroxenes dominate the Darwin type, whereas the Kimberley type contains significant amount of alkali feldspars. Despite the fact that they are alkali rich, they do not seem to contain feldspathoids, such as nepheline or leucite.

Conglomerates are composed of grains and clasts, likely transported from the igneous crust of Gale Crater's rim. Their composition is in agreement with most of the felsic alkali-rich float rocks analyzed in the hummocky plains (such as those reported in *Sautter et al. [2015]*), suggesting that most of the latter are local to the Gale Crater rim, with a few exceptions that may have been emplaced from further afield (e.g., ejecta of impacts). The average composition of conglomerates at Darwin can be taken as a proxy of the average igneous composition at Gale Crater. We propose to use the composition of the Darwin type as a representative average because the Kimberley type apparently represents an enrichment that is more local and less representative. The conglomerates at Gale Crater provide a window into the diverse crustal composition and likely igneous rocks in the vicinity of Gale. The varied compositions indicate distinct source regions, which included more typical average Mars, basaltic igneous rocks, alkali-rich (high Na + K) igneous rocks, and potassic igneous rocks. The fact that we do not detect the alkaline and potassic igneous rocks from orbit is probably twofold. First, the areal extent of these terrains may be limited and close to the resolution of the orbital spectrometers, and second, dust/soil cover can completely obscure the spectral signature of the underlying bedrock and bias results toward basaltic compositions and associated mineralogy. Our results suggest that Mars may have a far more varied near-surface crustal composition than has previously been suggested.

The conglomerate compositions are also compared to those of finer-grained deposits in the Yellowknife Bay formation, Kimberley formation, and the basal Murray formation at Pahrump Hills. The chemistry of finer-grained sediments is significantly different from that of conglomerates. Pahrump Hills fine-grained sediments

display a composition close to that of fluvial conglomerates, in agreement with a fluviolacustrine origin proposed from their facies [Grotzinger *et al.*, 2015]. Although also formed by fluviolacustrine processes, Yellowknife Bay formation sediments display a much higher mafic content that is not explainable by a single process: Physical sorting and Mg diagenetic fluids/cements may have played a role, but as their compositions are more mafic than a source rock similar to that of conglomerates, their sources may have included more mafic sediments such as wind-blown material. Lastly, the Kimberley formation fine-grained sediments are genetically related to the Kimberley-type conglomerates, but with noticeable variations, including a higher content of potassium. Thus, even if most of the sediments analyzed by the rover are detrital and come from the Gale Crater rim, the comparison between conglomerates and finer-grained sediments shows strong differences and suggests various modifications specific to each rock type and analyzed sites during and after deposition.

Appendix A: Instruments and Data

A1. Chemistry

The MSL APXS (Alpha-Particle X-Ray Spectrometer) uses radioactive ^{244}Cm sources that excite geologic samples via particle-induced X-ray emission and X-ray fluorescence. APXS is placed in contact or close proximity (<2 cm) to rocks. X-ray emissions are determined for each element of the analyzed target. Their intensities are used to determine the abundances of major, minor, and some trace (Cr, Ni, Zn, Br, and Ge) elements [Campbell *et al.*, 2012; Gellert *et al.*, 2013]. The errors reported in Table A1 for APXS are statistical analytical errors and represent precision (for corresponding data in Tables 3 and 4). These errors take into account variations of the spectral intensity (resulting from differences in the duration and standoff of APXS integrations), the temperature at which the analyses are obtained as well as the abundance of the element in question, and the concentration of the surrounding elements and the rock type. Best estimates of overall analytical accuracy errors for APXS are reported in Schmidt *et al.* [2014], and calibration efforts are ongoing.

The ChemCam instrument uses laser-induced breakdown spectroscopy (LIBS), a technique that uses a pulsed laser to ablate material from the rocks, producing a plasma [Wiens *et al.*, 2012; Maurice *et al.*, 2012]. The plasma emits an atomic emission spectrum, which is analyzed by three spectrometers in the UV (240–342 nm), violet (382–469 nm), and visible near-infrared (474–906 nm) spectral ranges. ChemCam spectrometers allow identification of the emission lines of the elements present in the rocks or soils targeted [e.g., Cremers and Radziemski, 1983, 2006], including all major elements (Si, Al, K, Na, Ca, Mg, Fe, and Ti) and a several minor and trace elements (Li, Mn, Cr, Zn, Ni, Sr, Rb, and Ba) [e.g., Cousin *et al.*, 2015; Ollila *et al.*, 2014; Lasue *et al.*, 2016]. Volatiles and halogens (O, S, P, H, Cl, and F) are more difficult to analyze, but they have been identified locally [Meslin *et al.*, 2013; Schröder *et al.*, 2015; Forni *et al.*, 2015a]. Carbon is detected in all targets analyzed and is interpreted as the contribution of atmospheric carbon dioxide to the observed plasma [Schröder *et al.*, 2015].

Multivariate analyses use a range of emission lines and compare them to those of known standards analyzed in a testbed [Clegg *et al.*, 2009; Wiens *et al.*, 2013]. Indeed, all major elements have several emission peaks within ChemCam spectral range. Most of data published to date used a calibration based on 69 targets acquired on Earth. A major recalibration was recently completed, expanding the spectral library from 69 to more than 450 standards (especially extending the suite of standards to more felsic minerals), enabling a more precise determination of major element abundances [Wiens *et al.*, 2015; Clegg *et al.*, submitted manuscript]. This new calibration was used for all data in this paper. The root-mean-square error of prediction (RMSEP) describes the mean accuracy of the measurements over a “test set” of standards chosen to have a distribution of compositions similar to the full training set. For the new database we do k-fold cross validation where we split the training set into five “folds” each of which includes many standards and hold one fold out at a time. The RMSEP that we report is for a sixth “fold” that is used as a test set. RMSEP is the prediction of an individual point to fit inside the given uncertainties. However, when averaging a number of points of the same targets, the precision of measurements (obtained from a standard deviation) is usually a better estimation of the uncertainty than the RMSEP because it measures the consistency of the data assuming the rock is homogeneous [Blaney *et al.*, 2015; Mangold *et al.*, 2015]. However, this method provides large standard deviations for heterogeneous rocks, as the measurement of the uncertainty is not made on the same point and includes the natural grain to grain variability. Using the standard

Table A1. Precision Errors for APXS Analyses of Tables 3 and 4

	SiO ₂	TiO ₂	Al ₂ O ₃	FeO	MgO	CaO	Na ₂ O	K ₂ O
Ruker	0.54	0.05	0.29	0.13	0.17	0.08	0.14	0.04
Bardin Bluffs Pebble	0.86	0.07	0.38	0.2	0.25	0.13	0.27	0.04
Bardin Matrix	0.54	0.03	0.29	0.2	0.08	0.06	0.14	0.02
Dragons Teeth	0.75	0.05	0.29	0.2	0.25	0.13	0.2	0.05
Kerguelen	0.64	0.05	0.29	0.2	0.17	0.1	0.2	0.04
Heimdall	0.64	0.05	0.29	0.2	0.17	0.11	0.2	0.04
Jum Jum	0.64	0.05	0.29	0.2	0.17	0.08	0.2	0.11
	P ₂ O ₅	SO ₃	Cl	Cr ₂ O ₃	MnO	Ni/ppm	Zn/ppm	Br/ppm
Ruker	0.09	0.05	0.02	0.01	0.01	5	5	5
Bardin Bluffs Pebble	0.07	0.20	0.08	0.00	0.03	45	35	20
Dragons Teeth	0.07	0.20	0.06	0.03	0.04	45	45	15
Heimdall	0.07	0.20	0.04	0.03	0.03	35	35	10
Jum Jum	0.05	0.15	0.05	0.03	0.03	30	40	10

deviation of the ~30 spectra of a single observation point is another method that enables one to determine the precision of the measurement, but it is also limited by the possible variability in mineralogy with depth (Clegg et al., submitted manuscript).

Univariate analysis is generally used for minor and trace elements [Ollila et al., 2014; Cousin et al., 2015]. Minor element abundances determined in this study include F, Li, Sr, and Mn. They were all measured by the univariate technique using known emission lines and calibrated using onboard calibration targets [Fabre et al., 2014] or in some cases with targets observed under a simulated Martian atmosphere in the laboratory [e.g., Forni et al., 2015a; Lanza et al., 2015].

Independent component analysis (ICA) is a computational technique for revealing hidden factors that underlie sets of random variables [Comon, 1994; Hyvärinen et al., 2001]. ICA plots are used to plot elements that are difficult to determine in absolute abundance, such as hydrogen. Quantification of hydrogen is a complex problem in LIBS due to its dependence on matrix effects (i.e., variations in optical and mechanical properties) [Sobron et al., 2012; Schröder et al., 2015]. ICA diagrams display scores in axes that correspond to uncalibrated, relative variations in the abundances of the plotted elements.

A2. Imaging

The ChemCam instrument provides context imaging with submillimeter spatial resolution thanks to the Remote Micro-Imager (RMI) [Wiens et al., 2012; Maurice et al., 2012; Le Mouélic et al., 2015]. Images are taken before and after each series of LIBS points. The RMI uses a grid a 1024 × 1024 pixels with a spatial sampling of ~0.04 mm/pixel to ~0.15 mm/pixel, at 2 and 7 m, respectively [Le Mouélic et al., 2015]. The MastCam instrument is composed of two cameras: MastCam-L with a 34 mm, focal length, and a 0.22 mrad/pixel resolution and MastCam-R with a 100 mm focal length and a 0.074 mrad/pixel resolution [Malin et al., 2010; Bell et al., 2012]. Both cameras use a 1600 × 1200 detector. The Bayer filter used for MastCam images matches the human eye closely in terms of color response [Bell et al., 2012]. The Mars Hand Lens Imager (MAHLI) is a color CCD camera that can focus over a range of distances from 2.1 cm to infinity [Edgett et al., 2012]. MAHLI was designed for investigating Mars surface rocks and soils at the hand lens scale. Images are 1600 by 1200 pixels with a spatial resolution reaching 14 μm/pixel at best [Edgett et al., 2012].

Appendix B: Grain Size Measurements on Selected Conglomerates

To aid in the characterization of the conglomerates, we focused on the grain size distribution of those with the highest-resolution imagery (MAHLI images) at the Darwin (Bardin Bluffs and Dragons Teeth) and Kylie outcrops (Jum Jum). Each target was evaluated by determining the size of resolvable grains. Grain size was measured using the NIH software package ImageJ [Schneider et al., 2012]. Grain size was determined by measuring the longest axis of every visible grain in the mosaic. This approach may underestimate grain size if the long axis of the grain is not visible [Yingst et al., 2013]. Grain sizes were binned according to the Wentworth scale [Wentworth, 1922] (pebble = 4–64 mm, granule = 2–4 mm, very coarse sand = 1–2 mm, coarse sand = 0.5–1 mm, medium sand = 0.25–0.5 mm, and fine sand = 0.125–0.25 mm). For all targets, grains

Table B1. Grain Measurement in Three Locations Where MAHLI Images Were Available

Target	Number of Measured Grains						
	Total Number	Pebble	Granule	Sand			
				Very Coarse	Coarse	Medium	Fine
Bardin Bluff	48	1	4	15	15	9	4
Dragons Teeth	26	4	5	13	4	0	0
Jum Jum	8	2	6	0	0	0	0

were defined either by color contrast between grains, which defined grain boundaries, or the grain having eroded out of the outcrop to reveal the edges of the grain boundaries, or both.

Accurate grain measurement can be difficult for very small grain sizes. Pixelation can blur grain edges, and grains smaller than several times the pixel projection size are not resolvable [Friday *et al.*, 2013]. Additionally, two-dimensional grain analysis is known to overestimate particle size in small grains (35–140 $\mu\text{m}/\text{pixel}$) [Fedo *et al.*, 2012]. To reduce possible error in grain size measurements, we required measured grains in this study to be composed of at least 5 pixels (as in Yingst *et al.* [2008]). We measured grain sizes in three conglomerate targets, Bardin Bluffs (sol 395, Darwin outcrop, Figure 4d), Dragons Teeth (sol 399, Darwin outcrop Figure 4e), and Jum Jum (sol 550 outcrop, Kylie outcrop, Figure 6), and applied a similar methodology to that utilized in Anderson *et al.* [2015] to characterize each target based partially on grain size. Measurable grain sizes range from fine sand to pebble (Table B1).

Bardin Bluff. Measured clasts ($n = 48$) range from fine sand to pebble and average 1.17 mm (very coarse sand). The measured grain size distribution is poorly sorted ($\phi = 1.10$). Grains smaller than 0.125 mm are likely present but neither measurable nor resolvable. The whole outcrop is poorly sorted.

Dragons Teeth. Measured clasts ($n = 26$) in Dragons Teeth range from coarse sand to pebble and average 2.05 mm (granule). The measured grain size distribution is moderately sorted ($\phi = 0.77$), although together with the smaller matrix particles, the whole outcrop is poorly sorted.

Jum Jum. Measured clasts ($n = 8$) range from granule to pebble and average 3.86 mm (granule). The measured grain size distribution is poorly sorted ($\phi = 1.45$). Smaller grains are likely present in the rock but are neither measurable nor resolvable. Grain identification is difficult because there is poor color contrast between grains in the rock due to dust and polished texture. Therefore, very few grains were resolvable and measured in the target.

To determine the proportion of small grains (<0.125 mm), a grid with 10 mm^2 dimensions was overlaid on the images to allow us an unbiased method to measure the variety of grains at every grid intersection without the need to measure every grain in the image. From the total number of potential measurements (grid intersection lines), points that were not resolvable (e.g., out of focus or no data) were subtracted from the total. Then the percentage of grains <0.125 mm was calculated. We found that both Bardin Bluff and Dragons Teeth (Figures 4d and 4e) have a proportion of visible grains $>90\%$, limiting the material finer than 0.125 mm to $<10\%$. Jum Jum has a polished texture that does not allow the same exercise, leaving open the possibility of a higher proportion of fines or cement.

Acknowledgments

We are grateful to Marjorie Chan and two anonymous reviewers for their insightful comments. Development and operation of the ChemCam instrument was supported in France by funds from the French space agency, Centre National d'Etudes Spatiales (CNES). Support for development and operation in the U.S. was provided by NASA to the Mars Exploration Program and specifically to the MSL team. The APXS is managed and financed by the Canadian Space Agency (CSA). Imaging and chemical data presented here are available in the NASA Planetary Data System (PDS) <http://pds-geosciences.wustl.edu/missions/msl>. We are grateful to the MSL engineering and management teams (and especially the Jet Propulsion Laboratory, California Institute of Technology, under contract with NASA) for making the mission and this scientific investigation possible and to science team members who contributed to mission operations.

References

- Agee, C. B., *et al.* (2013), Unique meteorite from Early Amazonian Mars: Water-rich basaltic breccia Northwest Africa 7034, *Science*, 339, 780–785.
- Anderson, R., *et al.* (2015), ChemCam results from the Shaler outcrop in Gale Crater, Mars, *Icarus*, 249, 2–21, doi:10.1016/j.icarus.2014.07.025.
- Bandfield, J. L., V. Hamilton, P. R. Christensen, and H. Y. McSween Jr. (2004), Identification of quartzofeldspathic materials on Mars, *J. Geophys. Res.*, 109, E10009, doi:10.1029/2004JE002290.
- Baratoux, D., H. Samuel, C. Michaut, M. J. Toplis, M. Monnereau, M. Wiczorek, R. Garcia, and K. Kurita (2014), Petrological constraints on the density and thickness of the Martian crust, *J. Geophys. Res. Planets*, 119, 1707–1727, doi:10.1002/2014JE004642.
- Bell, J. F., III, M. C. Malin, M. A. Caplinger, M. A. Ravine, A. S. Godber, M. C. Jungers, M. S. Rice, and R. B. Anderson (2012), Mastcam multispectral imaging on the Mars Science Laboratory rover: Wavelength coverage and imaging strategies at the Gale Crater field site, Proc. Lunar Planet. Sci. Conf. 43th, Abstract 2541.
- Berger, J. A., J. L. Campbell, K. S. Edgett, R. Gellert, P. L. King, G. M. Perrett, I. Pradler, M. Schmidt, and MSL Science Team (2013), A unique measurement of Martian dust by the Alpha Particle X-Ray Spectrometer on Curiosity in Gale Crater, Mars, *Geol. Soc. Am. Bull.*, 45(7), 138.
- Blaney, D. L., *et al.* (2015), Chemo-stratigraphy at the Pahrump outcrop and Garden City Vein Complex in Gale Crater using ChemCam, Euro. Planet. Sci. Conf., Nantes, Vol. 10, EPSC2015-391.

- Campbell, J. L., G. M. Perrett, R. Gellert, S. M. Andrushenko, N. L. Boyd, J. A. Maxwell, P. L. King, and C. D. M. Schofield (2012), Calibration of the Mars Science Laboratory Alpha Particle X-ray Spectrometer, *Space Sci. Rev.*, *170*, 319–340.
- Carter, J., and F. Poulet (2013), Ancient plutonic processes on Mars inferred from the detection of possible anorthositic terrains, *Nat. Geosci.*, *6*, 1008–1012.
- Cerny, P., R. E. Meintzer, and A. J. Anderson (1985), Extreme fractionation in rare-element pegmatites: Selected examples of data and mechanisms, *Can. Mineral.*, *23*, 381–421.
- Christensen, P. R., et al. (2005), Evidence for magmatic evolution and diversity on Mars from infrared observations, *Nature*, *436*, 504–509.
- Clegg, S. M., E. Sklute, M. D. Dyar, J. E. Barefield, and R. C. Wiens (2009), Multivariate analysis of remote laser-induced breakdown spectroscopy spectra using partial least squares, principal component analysis, and related techniques, *Spectrochim. Acta, Part B*, *64*, 79–88.
- Comon, P. (1994), Independent component analysis: A new concept? *Signal Process.*, *36*, 287–314.
- Cousin, A., et al. (2015), Compositions of coarse and fine particles in Martian soils at Gale: A window into the production of soils, *Icarus*, *249*, 22–42, doi:10.1016/j.icarus.2014.04.052.
- Cox, R., and D. Lowe (1995), A conceptual review of regional-scale controls of the composition of clastic sediment and the co-evolution of continental blocks and their sedimentary cover, *J. Sediment. Res.*, *A65*(1), 1–12.
- Cremers, D. A., and L. J. Radziemski (1983), Detection of fluorine and chlorine in air by laser-induced breakdown spectroscopy, *Anal. Chem.*, *55*, 1252–1256.
- Cremers, D. A., and L. J. Radziemski (2006), *Handbook of Laser-Induced Breakdown Spectroscopy*, 292 pp., Wiley, Chichester, U. K.
- Dehouck, E., and S. M. McLennan (2015), Evaluating the homogeneity of the X-Ray amorphous component along the Curiosity rover traverse, *Eur. Planet. Sci. Conf.*, Nantes, *10*, 327.
- Dehouck, E., S. M. McLennan, P.-Y. Meslin, and A. Cousin (2014), Constraints on abundance, composition, and nature of X-ray amorphous components of soils and rocks at Gale Crater, Mars, *J. Geophys. Res. Planets*, *119*, 2640–2657, doi:10.1002/2014JE004716.
- Drake, M. J., and D. F. Weill (1975), Partition of Sr, Ba, Ca, Y, Eu²⁺, Eu³⁺, and other REE between plagioclase feldspar and magmatic liquid: An experimental study, *Geochim. Cosmochim. Acta*, *39*, 689–712.
- Edgar, L. A., et al. (2014), Cross-bedded facies and inferred paleocurrents observed by the Curiosity rover along the traverse to Mt. Sharp, Gale Crater, Mars, Mars Conf. 8th, Pasadena, Abstract 1389.
- Edgett, K. S., et al. (2012), Curiosity's Mars Hand Lens Imager (MAHLI) investigation, *Space Sci. Rev.*, *170*, 259–317.
- Elkins-Tanton, L. T., E. M. Parmentier, and P. C. Hess (2005), The formation of ancient crust on Mars through magma ocean processes, *J. Geophys. Res.*, *110*, E12S01, doi:10.1029/2005JE002480.
- Fabre, C., et al. (2014), In situ calibration using univariate analyses based on the onboard ChemCam targets: First prediction of Martian rock and soil compositions, *Spectrochim. Acta, Part B*, *99*, 34–51, doi:10.1016/j.sab.2014.03.014.
- Fedo, C. M., M. E. Friday, I. O. McGlynn, and H. Y. McSween (2012), Resolving basaltic sediment characteristics from 2D images using known 3D data: Implications for describing and interpreting the Martian surface, *Geol. Soc. of Am., Abstracts with Programs* *44*: 403.
- Fedo, C. M., I. O. McGlynn, and H. Y. McSween Jr. (2015), Grain size and hydrodynamic sorting controls on the composition of basaltic sediments: Implications for interpreting Martian soils, *Earth Planet. Sci. Lett.*, *423*, 67–77.
- Forni, O., et al. (2015a), First detection of fluorine on Mars: Implications for Gale Crater's geochemistry, *Geophys. Res. Lett.*, *42*, 1020–1028, doi:10.1002/2014GL062742.
- Forni, O., et al. (2015b), Fluorine and lithium at the Kimberley outcrop, Gale Crater, Proc. Lunar Planet. Sci. Conf. 46th, The Woodlands, Tex., LPI, Abstract 1832.
- Friday, M. E., C. M. Fedo, I. O. McGlynn, and H. Y. McSween (2013), The accuracy of 2D assessment of sediment textures, and application to Mars, Proc. Lunar Planet. Sci. Conf., Abstract 2361.
- Gellert, R., et al. (2013), Initial MSL APXS activities and observations at Gale Crater, Mars, Proc. Lunar Planet. Sci. Conf. 44th, Abstract 1432.
- Grotzinger, J. P., et al. (2014), A habitable fluvio-lacustrine environment at Yellowknife Bay, Gale Crater, Mars, *Science*, *343*, doi:10.1126/science.1242777.
- Grotzinger, J. P., et al. (2015), Deposition, exhumation, and paleoclimate of an ancient lake deposit, Gale Crater, Mars, *Science*, *350*(6257), doi:10.1126/science.aac7575.
- Hamilton, V. E., and P. R. Christensen (2005), Evidence for extensive, olivine-rich bedrock on Mars, *Geology*, *33*, 433–436.
- Humayun, M., et al. (2013), Origin and age of the earliest Martian crust from meteorite NWA7533, *Nature*, *503*, 513–517.
- Hyvärinen, A., J. Karhunen, and E. Oja (2001), *Independent Component Analysis*, pp. 480, Wiley, New York.
- Kiminami, K., and K. Fujii (2007), The relationship between major element concentration and grain size within sandstones from four turbidite sequences in Japan, *Sediment. Geol.*, *195*, 203–215.
- Lanza, N., et al. (2015), Oxidation of manganese at Kimberley, Gale Crater: More free oxygen in Mars past?, LPSC 46th, Houston, Abstract 289.
- Lasue, J., S. M. Clegg, O. Forni, A. Cousin, R. C. Wiens, N. Lanza, N. Mangold, O. Gasnault, S. Maurice, and the MSL Science team (2015), Detection of Zn with ChemCam on Mars, LPSC 46th, Abstract 1413.
- Lasue, J., et al. (2016), Observation of > 5 wt % zinc by ChemCam LIBS at the Kimberley, Gale Crater, Mars, *J. Geophys. Res. Planets*, *121*, doi:10.1002/2015JE004946, in press.
- Le Deit, L., et al. (2014), Chemical composition and texture of Cooperstown outcrops in Gale Crater as seen by ChemCam on Curiosity, Int. Conf. on Mars 8th, Pasadena, Abstract 1216.
- Le Deit, L., et al. (2015), The potassic sedimentary rocks in Gale Crater, Mars as seen by ChemCam onboard Curiosity, Proc. Lunar Planet. Sci. Conf. XLVI, The Woodlands, Tex., Abstract 1438.
- Le Mouélic, S., et al. (2015), The ChemCam Remote Micro-Imager at Gale Crater: Review of the first year of operations on Mars, *Icarus*, *249*, 93–107, doi:10.1016/j.icarus.2014.05.030.
- Leberkmo, J. F., and F. A. Campbell (1969), Distribution, composition and source of the White River ash, Yukon Territory, *Can. J. Earth. Sci.*, *6*, 109–116.
- Leeder, M. (1999), *Sedimentology and Sedimentary Basins*, pp. 592, Blackwell Science, Oxford, U. K.
- Léveillé, R., et al. (2014), Chemistry of fracture-filling raised ridges in Yellowknife Bay, Gale Crater: Window into past aqueous activity and habitability on Mars, *J. Geophys. Res. Planets*, *119*, 2398–2415, doi:10.1002/2014JE004620.
- Malin, M. C., et al. (2010), The Mars Science Laboratory (MSL) Mast-mounted Cameras (Mastcams) flight instruments, Proc. Lunar Planet. Sci. Conf. 41th, Abstract 1123.
- Mangold, N., et al. (2010), Mineralogy of recent volcanic plains in the Tharsis region, Mars, and implications for platy-ridged flow composition, *Earth Planet. Sci. Lett.*, *294*(3–4), 440–450, doi:10.1016/j.epsl.2009.07.036.
- Mangold, N., D. Baratoux, O. Arnalds, J.-M. Bardintzeff, B. Platevoet, M. Grégoire, and P. Pinet (2011), Segregation of olivine grains in volcanic sands in Iceland and implications for Mars, *Earth Planet. Sci. Lett.*, *310*, 233–243.

- Mangold, N., et al. (2015), Chemical variations in Yellowknife Bay formation sedimentary rocks analyzed by ChemCam onboard the Curiosity rover on Mars, *J. Geophys. Res. Planets*, *120*, 452–482, doi:10.1002/2014JE004681.
- Maurice, S., et al. (2012), The ChemCam instrument suite on the Mars Science Laboratory (MSL) rover: Science objectives and mast unit description, *Space Sci. Rev.*, *170*, 95–166, doi:10.1007/s11214-012-9912-2.
- McCanta, M. C., P. A. Dobosh, M. D. Dyar, and H. E. Newsom (2013), Testing the veracity of LIBS analyses on Mars using the LIBSSIM program, *Planet. Space Sci.*, *81*, 48–54.
- McLennan, S. M., S. R. Taylor, M. T. McCulloch, and J. B. Maynard (1990), Geochemical and Nd/Sr isotopic composition of deep-sea turbidites: Crustal evolution and plate tectonic associations, *Geochim. Cosmochim. Acta*, *54*(7), 2015–2050.
- McLennan, S. M., S. Hemming, D. K. McDaniel, and G. N. Hanson (1993), Geochemical approaches to sedimentation, provenance, and tectonics, in *Processes Controlling the Composition of Clastic Sediments*, *Geol. Soc. Am. Spec. Pap.*, vol. 284, edited by M. J. Johnsson and A. Basu, pp. 21–40.
- McLennan, S. M., et al. (2014), Elemental geochemistry of sedimentary rocks in Yellowknife Bay, Gale Crater, Mars, *Science*, *343*, doi:10.1126/science.1244734.
- McSween, H. Y., Grove, T. L., and Wyatt, M. B. (2003), Constraints on the composition and petrogenesis of the Martian crust, *J. Geophys. Res.*, *108*(E12), 5135, doi:10.1029/2003JE002175.
- McSween, H. Y., et al. (2006), Alkaline volcanic rocks from the Columbia Hills, Gusev crater, Mars, *J. Geophys. Res.*, *111*, E09S91, doi:10.1029/2006JE002698.
- McSween, H. Y., G. J. Taylor, and M. B. Wyatt (2009), Elemental composition of the Martian crust, *Science*, *324*, 736–739.
- Melosh, H. J. (1989), *Impact Cratering as a Geological Process*, *Oxford Monogr. Geol. Geophys.*, Oxford Univ. Press, New York.
- Meslin, P.-Y., et al. (2013), Soil diversity and hydration as observed by ChemCam at Gale Crater, Mars, *Science*, *341*, doi:10.1126/science.1238670.
- Mustard, J. F., F. Poulet, A. Gendrin, J.-P. Bibring, Y. Langevin, B. Gondet, N. Mangold, G. Bellucci, and F. Altieri (2005), Olivine and pyroxene diversity in the crust of Mars, *Science*, *307*, 1594–1597, doi:10.1126/science.1109098.
- Mustard, J. F., F. Poulet, J. W. Head, N. Mangold, J.-P. Bibring, S. M. Pelkey, C. Fassett, Y. Langevin, and G. Neukum (2007), Mineralogy of the Nili Fossae region with OMEGA/Mex data: 1. Ancient impact melt in the Isidis Basin and implications for the transition from the Noachian to Hesperian, *J. Geophys. Res.*, *112*, E08S03, doi:10.1029/2006JE002834.
- Nachon, M., et al. (2015), Diagenetic features analyzed by Chemcam/Curiosity at Pahrump Hills, Gale Crater, Mars, Proc. Lunar Planet. Sci. Conf. 46th, Houston, Abstract 1524.
- Ody, A., F. Poulet, Y. Langevin, J.-P. Bibring, G. Bellucci, F. Altieri, B. Gondet, M. Vincendon, J. Carter, and N. Manaud (2012), Global maps of anhydrous minerals at the surface of Mars from OMEGA/Mex, *J. Geophys. Res.*, *117*, E00J14, doi:10.1029/2012JE004117.
- Ollila, A., et al. (2014), Trace element geochemistry (Li, Ba, Sr, and Rb) using Curiosity's ChemCam: Early results for Gale Crater from Bradbury Landing site to Rocknest, *J. Geophys. Res. Planets*, *119*, 18–31, doi:10.1002/2013JE004517.
- Palucis, M., W. Dietrich, A. Hayes, R. Williams, S. Gupta, N. Mangold, H. E. Newsom, C. Hardgrove, F. Calef, and D. Sumner (2014), The origin and evolution of the Peace Vallis fan system that drains to the Curiosity landing area, Gale Crater, Mars, *J. Geophys. Res. Planets*, *119*, 705–728, doi:10.1002/2013JE004583.
- Poulet, F., et al. (2009), Quantitative compositional analysis of Martian mafic regions using the Mex/OMEGA reflectance data: 2. Petrological implications, *Icarus*, *201*, 84–101.
- Sautter, V., et al. (2014), Igneous mineralogy at Bradbury rise: The first ChemCam campaign, *J. Geophys. Res. Planets*, *119*, 1–31, doi:10.1002/2013JE004472.
- Sautter, V., et al. (2015), In situ evidence for continental crust on early Mars, *Nat. Geosci.*, doi:10.1038/ngeo2474.
- Schmidt, M. E., et al. (2014), Geochemical diversity in first rocks examined by the Curiosity Rover in Gale Crater: Evidence for and significance of an alkali and volatile-rich igneous source, *J. Geophys. Res. Planets*, *119*, 64–81, doi:10.1002/2013JE004481.
- Schneider, C. A., W. S. Rasband, and K. W. Elceiri (2012), NIH Image to ImageJ: 25 years of image analysis, *Nat. Methods*, *9*, 671–675.
- Schröder, S., et al. (2015), Hydrogen detection with ChemCam spectra at Gale Crater, Mars, *Icarus*, doi:10.1016/j.icarus.2014.08.029.
- Seiders, V. M., and C. D. Blome (1988), Implications of upper Mesozoic conglomerate for suspect terranes in western California and adjacent areas, *Geol. Soc. Am. Bull.*, *100*, 374–391.
- Siebach, K., et al. (2015), Sorting out APXS compositional variations in Gale Crater sedimentary rocks, Mars, Geol. Soc. Am. Ann. Meeting, Baltimore, 94-2.
- Sobron, P., A. Wang, and F. Sobron (2012), Extraction of compositional and hydration information of sulfates from laser-induced plasma spectra recorded under Mars atmospheric conditions—Implications for ChemCam investigations on Curiosity rover, *Spectrochim. Acta, Part B*, *68*, 1–16.
- Stack, K. M., J. P. Grotzinger, D. Y. Sumner, F. Calef, L. A. Edgar, S. Gupta, K. Lewis, M. S. Rice, D. M. Rubin, and R. M. E. Rebecca (2014), Synthesizing MSL Curiosity rover observations and orbital geologic mapping to build a regional stratigraphy for Aeolis Palus, GSA Annual Meeting, Vancouver, Canada, 19–22 October 2014, Abstract 245505.
- Stöffler, D., H. D. Knöll, and U. März (1979), Terrestrial and lunar impact breccias and the classification of lunar highland rocks, Proc. Lunar Planet. Sci. Conf. 10th, 639–675.
- Stolper, E., et al. (2013), The petrochemistry of Jake Matijevic: A Martian Mugarite, *Science*, *341*, doi:10.1126/science.1239463.
- Szabo, T., G. Domokos, J. P. Grotzinger, and D. Jerolmack (2015), Reconstructing the transport history of pebbles on Mars, *Nat. Commun.*, *6*, 8366, doi:10.1038/ncomms9366.
- Taylor, G. J., L. M. V. Martel, S. Karunatillake, O. Gasnault, and W. V. Boynton (2010), Mapping Mars geochemically, *Geology*, *38*(2), 183–186.
- Taylor, S. R., and S. M. McLennan (1995), The geochemical evolution of the continental crust, *Rev. Geophys.*, *33*, 241–265, doi:10.1029/95RG00262.
- Taylor, S. R., and S. M. McLennan (2009), *Planetary Crusts*, 378 pp., Cambridge Univ. Press, Cambridge, U. K.
- Thompson, L. M., M. E. Schmidt, G. Perrett, B. Elliott, R. Gellert, and M. Fisk (2014), K-rich rocks at Gale, Dingo Gap to the Kimberley: An APXS perspective, Int. Conf. on Mars 8th, Pasadena, Calif., No. 1791, p.1433.
- Thompson, L. M., R. Gellert, J. G. Spray, L. C. Kah, and the APXS and MSL Science Teams (2015), The composition of the basal Murray Formation at Pahrump Hills, Gale Crater, Mars, Proc. Lunar Planet. Sci. Conf. 46th, Houston, Abstract 1429.
- Treiman, A., et al. (2016), Mineralogy, provenance, and diagenesis of a potassic basaltic sandstone on Mars: ChemMin X-ray diffraction of the Windjana sample (Kimberley area, Gale Crater), *J. Geophys. Res. Planets*, *121*, 75–106, doi:10.1002/2015JE004932.
- Vaniman, D., et al. (2014), Mineralogy of a mudstone at Yellowknife Bay, Gale Crater, Mars, *Science*, *343*, doi:10.1126/science.1243480.
- Vasavada, A. R., et al. (2014), Overview of the Mars Science Laboratory mission: Bradbury Landing to Yellowknife Bay and beyond, *J. Geophys. Res. Planets*, *119*, 1134–1161, doi:10.1002/2014JE004622.
- Wentworth, C. K. (1922), A scale of grade and class terms for clastic sediments, *J. Geol.*, *30*, 377–392.
- Wiens, R. C., et al. (2012), The ChemCam instrument suite on the Mars Science Laboratory (MSL) rover: Body unit and combined system tests, *Space Sci. Rev.*, 167–227, doi:10.1007/s11214-012-9902-4.

- Wiens, R. C., et al. (2013), Pre-flight calibration and initial data processing for the ChemCam laser-induced breakdown spectroscopy instrument on the Mars Science Laboratory rover, *Spectrochim. Acta, Part B*, *82*, 1–27.
- Wiens, R. C., et al. (2015), AGU Major-element compositional diversity observed by ChemCam along the MSL traverse: The first three years, Abstract 43B-2124.
- Williams, R. M. E., et al. (2013), Martian fluvial conglomerates at Gale Crater, *Science*, *340*, 1068–1072, doi:10.1126/science.1237317.
- Williams, R. M. E., et al. (2014), Sedimentology of Darwin waypoint from Curiosity observations, Proc. Lunar Planet. Sci. Conf. 45th, Abstract 2401.
- Wittmann, A., R. L. Korotev, B. L. Jolliff, A. J. Irving, D. E. Moser, I. Barker, and D. Rumble (2015), Petrography and composition of Martian regolith breccia meteorite Northwest Africa 7475, *Meteorit. Planet. Sci.*, *50*, 326–352.
- Wray, J. J., S. T. Hansen, J. Dufek, G. A. Swayze, S. L. Murchie, F. P. Seelos, J. R. Skok, R. P. Irwin III, and M. S. Ghiorso (2013), Prolonged magmatic activity on Mars inferred from the detection of felsic rocks, *Nat. Geosci.*, *6*, 1013–1017.
- Yingst, R. A., L. Crumpler, W. H. Farrand, R. Li, N. A. Cabrol, and L. D. Neakrase (2008), Morphology and texture of particles along the Spirit rover traverse from sol 450 to sol 745, *J. Geophys. Res.*, *113*, E12S41, doi:10.1029/2008JE003179.
- Yingst, R. A., et al. (2013), Characteristics of pebble- and cobble-sized clasts along the Curiosity rover traverse from Bradbury Landing to Rocknest, *J. Geophys. Res. Planets*, *118*, 2361–2380, doi:10.1002/2013JE004435.